Fermi Large Area Telescope First Source Catalog

The *Fermi* LAT Collaboration

ABSTRACT

We present a catalog of high-energy gamma-ray sources detected by the Large Area Telescope (LAT) on the *Fermi Gamma-ray Space Telescope (Fermi)* mission during the first 11 months of the science phase of the mission, which began on 2008 August 4. The 1FGL catalog contains 1451 sources detected and characterized in the 100 MeV to 100 GeV range. Source detection was based on the average flux over the 11-month period, and the threshold likelihood Test Statistic is 25, corresponding to a significance of just over 4 σ. The First Fermi LAT catalog includes source location regions, defined in terms of elliptical fits to the 95% confidence regions and power-law spectral fits as well as flux measurements in 5 bands for each source. In addition, monthly light curves are provided. We have evaluated the populations of gamma-ray sources that are represented in the catalog using a protocol defined before launch. For individual LAT-detected sources we provide identifications or plausible associations with sources in other astronomical catalogs. For the catalogs and association criteria that we have selected, 690 of the sources are unassociated. Care was taken to characterize the sensitivity of the results to the model of interstellar diffuse gamma-ray emission used to model the bright foreground, and 163 sources at low Galactic latitudes and toward bright local interstellar clouds are flagged as having positions that are strongly dependent on the model or as potentially entirely due to incorrectly modeled structure in the Galactic diffuse emission.

Subject headings: Gamma rays: observations — surveys — catalogs; Fermi Gamma-ray Space Telescope; PACS: 95.85.Pw, 98.70.Rz

1. Introduction

The *Fermi Gamma-Ray Space Telescope* mission has been routinely surveying the sky with the Large Area Telescope (LAT) since the science phase of the mission began in 2008

August. The combination of deep and fairly uniform exposure, good per-photon angular resolution, and stable response of the LAT have made for the most sensitive, best-resolved survey of the sky so far in the GeV energy range.

Observations at these high energies reveal non-thermal sources and a wide range of processes by which Nature accelerates particles. The utility of a uniformly-analyzed catalog such as the present one is both for identifying special sources of interest for further study and for characterizing populations of γ-ray emitters. The LAT survey data analyzed here allow much more detailed characterizations of variability and spectral shapes than has been possible before.

Here we expand on the Bright Source List (Abdo et al. 2009k, , BSL), which was an early release of 205 high-significance (likelihood Test Statistic $TS > 100$; see § 4.3) sources detected with the first 3 months of science data. The expansion is in terms of time interval considered (11 months vs. 3 months), energy range (100 MeV – 100 GeV vs. 200 MeV – 100 GeV) significance threshold ($TS > 25$ vs. $TS > 100$), and detail provided for each source. Regarding the latter, we provide elliptical fits to the confidence regions for source location (vs. radii of circular approximations), fluxes in 5 bands (vs. 2 for the BSL) for the range 100 MeV – 100 GeV, and monthly light curves for the integral flux over that range.

We also provide associations with previous γ-ray catalogs, for EGRET (Hartman et al. 1999; Casandjian & Grenier 2008) and AGILE (Pittori et al. 2009), and with likely counterpart sources from known or suspected source classes. The number of sources for which no plausible associations are found is 690, and we also investigate briefly the properties of these sources.

As with the BSL, the First *Fermi* LAT Catalog of gamma-ray sources (1FGL, for first Fermi Gamma-ray LAT) is not flux limited and hence not uniform. As described in § 4, the sensitivity limit depends on the region of the sky and on the hardness of the spectrum. Only sources with $TS > 25$ (corresponding to 4.1 σ statistical significance) are included, as described below.

2. Gamma-ray Detection with the Large Area Telescope

The LAT is a pair-production telescope (Atwood et al. 2009). The tracking section has 36 layers of silicon strip detectors to record the tracks of charged particles, interleaved with 16 layers of tungsten foil (12 thin layers, 0.03 radiation length, at the top or *Front* of the instrument, followed by 4 thick layers, 0.18 radiation length, in the *Back* section) to promote γ-ray pair conversion. Below the tracker lies an array of CsI crystals to determine the γ-ray

energy. The tracker is surrounded by segmented charged-particle anticoincidence detectors (plastic scintillators with photomultiplier tubes) to reject cosmic-ray background events. The LAT's improved sensitivity compared to EGRET stems from a large peak effective area ($\sim$8000 cm^2, or $\sim$6 times greater than EGRET's), large field of view ($\sim$2.4 sr, or nearly 5 times greater than EGRET's), good background rejection, superior angular resolution (68% containment angle $\sim 0.6°$ at 1 GeV for the *Front* section and about a factor of 2 larger for the *Back* section, vs. $\sim$1.7° at 1 GeV for EGRET; Thompson et al. 1993), and improved observing efficiency (keeping the sky in the field of view with scanning observations, vs. inertial pointing for EGRET). Pre-launch predictions of the instrument performance are described in Atwood et al. (2009).

The data analyzed for this Catalog were obtained during 2008 August 4 – 2009 July 4 (LAT runs 239557414 through 268411953, where the numbers refer to the Mission Elapsed Time (MET) in seconds since 00:00 UTC on 1 January 2001, at the start of the runs). During most of this time *Fermi* was operated in sky scanning survey mode (viewing direction rocking 35° north and south of the zenith on alternate orbits. During May 7–20 the rocking angle was increased to 39° for operational reasons. In addition, a few hours of special calibration observations during which the rocking angle was much larger than nominal for survey mode or the configuration of the LAT was different from normal for science operations were obtained during the period analyzed. Time intervals when the rocking angle was larger than 43° have been excluded from the analysis, because the bright limb of the Earth enters the field of view (see below).

In addition, two short time intervals associated with gamma-ray bursts (GRB) that were detected in the LAT have been excluded. These intervals correspond to GRB 080916C (MET 243216749–243217979, Abdo et al. 2009i) and GRB 081024B (MET 246576157–246576187).

Observations were nearly continuous during the survey interval, although a few data gaps are present due to operational issues, special calibration runs, or in rare cases, data loss in transmission. Table 1 lists all data gaps longer than 1 h. The longest gap by far is 3.9 d starting early on March 16; together the gaps longer than 1 h amount to $\sim$7.9 d or 2.4% of the interval analyzed for the 1FGL Catalog.

The total live time included is 245.6 d (21.22 Ms). This corresponds to an absolute efficiency of 73.5%. Most of the inefficiency is due to time lost during passages through the South Atlantic Anomaly ($\sim$13%) and to readout dead time (9.2%).

The standard onboard filtering, event reconstruction, and classification were applied to

Table 1.   Gaps Longer Than One Hour in Data

Start of Gap (UTC)	Duration (h)
2008-09-30 14:27	1.16
2008-10-11 03:14	1.59
2008-10-11 11:04	3.82
2008-10-14 12:23	3.83
2008-10-14 17:11	3.49
2008-10-14 20:22	1.59
2008-10-15 17:03	3.47
2008-10-16 15:18	1.83
2008-10-22 19:20	1.59
2008-10-22 23:43	2.06
2008-10-23 11:16	1.91
2008-10-30 16:43	1.59
2008-12-11 17:41	6.37
2009-01-01 00:35	1.72
2009-01-06 20:43	6.98
2009-01-13 13:26	2.10
2009-01-17 12:58	2.05
2009-01-28 19:28	4.78
2009-02-01 15:46	1.59
2009-02-15 10:15	1.05
2009-03-16 00:27	116.78
2009-05-02 19:04	8.94
2009-05-07 15:21	5.46
2009-06-26 12:59	3.19

the data (Atwood et al. 2009), and for this analysis the 'Diffuse' event class[1] is used. This is the class with the least residual contamination from charged-particle background events, released to the public. The tradeoff for using this event class relative to the 'looser' Source class is primarily reduced effective area, especially below 500 MeV.

The instrument response functions (IRFs) – effective area, energy redistribution, and point-spread function (PSF) – used in the likelihood analyses described below were derived from GEANT4-based Monte Carlo simulations of the LAT using the event selections corresponding to the Diffuse event class. The Monte Carlo simulations themselves were calibrated prior to launch using accelerator tests of flight-spare 'towers' of the LAT (Atwood et al. 2009) and have since been updated based on observation of pile up effects on the reconstruction efficiency in flight data Rando et al. (2009). The effect introduces an inefficiency that is proportional to the trigger rate and dependent on energy. The Catalog analysis uses the P6_V3 IRFs, which have the effective areas corrected for the inefficiency corresponding to the overall average trigger rate seen by the LAT, and Diffuse-class events are used. With the P6_V3 IRFs we extend the Catalog analysis down to 100 MeV (vs. 200 MeV for the BSL analysis, which used P6_V1). Below 100 MeV the effective area is relatively small and strongly dependent on energy. These considerations, together with the increasing breadth of the PSF at low energies (scaling approximately as $0.8°(E/1\mathrm{GeV})^{-0.8}$), motivated the selection of 100 MeV as the lower limit for this analysis.

The alignment of the *Fermi* observatory viewing direction with the z-axis of the LAT was found to be stable during survey-mode observation (Abdo et al. 2009o). Analyses of flight data suggest that the PSF is somewhat broader than the calculated Diffuse class PSF at energies greater than ∼10 GeV; the primary effect for the current analysis is to decrease the localization capability somewhat. As discussed below, this is taken into account in the Catalog by increasing the derived sizes of source location regions by 10%.

For the analysis, a cut on zenith angle was applied to the Diffuse class events to limit the contamination from albedo γ-rays from interactions of cosmic rays with the upper atmosphere of the Earth. These interactions make the limb of the Earth (zenith angle ∼113° at the 565 km, nearly-circular orbit of *Fermi*) an intensely-bright γ-ray source (Thompson et al. 1981). The limb is very far off axis in survey mode observations, at least 70° for the data set considered here. Removing events at zenith angles greater than 105° affects the exposure calculation negligibly but reduces the overall background rate. After these cuts, the data set contains 1.1×10^7 Diffuse-class events with energies >100 MeV.

The intensity map of Figure 1 summarizes the data set used for this analysis and shows

---

[1]See http://fermi.gsfc.nasa.gov/ssc/data/analysis/documentation/Cicerone/Cicerone_Data/LAT_DP.html.

the dramatic increase at low Galactic latitudes of the brightness of the γ-ray sky. The corresponding exposure is relatively flat and featureless as for the shorter time interval analyzed for the BSL. The exposure nonuniformities are relatively small (about 30% difference between minimum and maximum), with the deficit around the south celestial pole due to loss of exposure during passages of *Fermi* through the South Atlantic Anomaly (Atwood et al. 2009).

3.   Diffuse emission model

As mentioned in § 4, an essential input to the analyses for detecting and characterizing gamma-ray sources in the LAT data is a model of the diffuse gamma-ray intensity of the sky. Interactions between cosmic rays and interstellar gas and photons make the Milky Way a bright, structured celestial foreground. Unresolved emission from extragalactic sources contributes an isotropic component as well. In addition, residual charged-particle background, i.e., cosmic rays that trigger the LAT and are misclassified as gamma rays, provides another approximately isotropic background. For the analyses described in this paper we used models for the Galactic diffuse emission (`gll_iem_v02.fit`) and isotropic backgrounds that were developed by the LAT team and made publicly available as models recommended for high-level analyses.

Briefly, the model for the Galactic diffuse emission was developed using spectral line surveys of H I, CO (as a tracer of H_2) to derive the distribution of interstellar gas in Galactocentric rings. Infrared tracers of dust column density were used to correct column densities as needed, e.g., in directions where the optical depth of H I was either over or under-estimated. The model of the diffuse gamma-ray emission was then constructed by fitting the gamma-ray emissivities of the rings in several energy bands to the LAT observations. The fitting also required a model of the inverse Compton emission that was calculated using GALPROP (Strong et al. 2004; Strong 2007) and a model for the isotropic diffuse emission.

The isotropic component was derived as the residual of a fit of the Galactic diffuse emission model to the LAT data at Galactic latitudes above $|b| = 30\,°$ and so by construction includes the contribution of residual (misclassified) cosmic rays for the event analysis class used (Pass 6 Diffuse; see § 2). Treating the residual charged particles as effectively an isotropic component of the gamma-ray sky brightness rests on the assumption that the acceptance for residual cosmic rays is the same as for gamma rays. This approximation has been found to be quite good, i.e., resulting in small residuals for model fitting in likelihood analysis, and the residual charged particles.

The models, along with descriptions of their derivation, are available from the *Fermi* Science Support Center[2].

4. Construction of the Catalog

The procedure followed to build the 1FGL catalog follows the same steps described in Abdo et al. (2009k) for the BSL, with a number of improvements. We recall those steps in this section, highlighting what was done differently for 1FGL.

The source list was built on the basis of the full time interval. That is, we did not attempt to detect potentially flaring sources on shorter time scales, beyond what is done routinely in the Automated Science Processing (Atwood et al. 2009). All bright flaring sources that were reported via Astronomer's Telegrams were also bright enough to be detected over 11 months, and are included in the 1FGL catalog anyway.

Three steps were applied in sequence: detection, localization, significance estimation. In this scheme the threshold for inclusion in 1FGL is defined at the last step, but the completeness is controlled by the first one. After the list was defined we determined the source characteristics (flux in 5 energy bands, time variability) and we searched for possible counterparts. The 1FGL catalog includes much more information for each source than the BSL. In what follows, flux F means photon flux and spectral index Γ is for photons (i.e., $F \propto E^{-\Gamma}$).

The pulsars (Abdo et al. 2009n) and X-ray binaries (Abdo et al. 2009h,l,m) which are identified via their rotation or orbital period, were detected and localized as ordinary sources. But they were entered explicitly at their true positions in the main maximum likelihood analysis (§ 4.3), in order not to bias their characteristics and those of their surroundings if the Galactic diffuse model is imperfect (§ 3). For the LAT-detected pulsars, we used the timing localization (Camilo et al. 2009; Weltevrede et al. 2010) which is always more precise than that based on the spatial distribution of the events. We have checked that the positions of the brightest pulsars found by the localization algorithm (§ 4.2) were consistent with their true positions at the 95% level (using only the statistical error, without any systematic correction).

---

[2]http://fermi.gsfc.nasa.gov/ssc.

4.1. Detection

The detection step used the same ideas that were detailed in Abdo et al. (2009k). It was based on the same three energy bands, combining *Front* and *Back* events to preserve spatial resolution. The detection does not use events below 200 MeV which have poor angular resolution. It uses events up to 100 GeV. The full band (6.7×10^6 counts) starts at 200 MeV for *Front* and 400 MeV for *Back* events. The medium band (12.0×10^5 counts) starts at 1 GeV for *Front* and 2 GeV for *Back* events. The hard band (10.7×10^4 counts) starts at 5 GeV for *Front* and 10 GeV for *Back* events.

We used the same partitioning of the sky using 24 planar projections as in the BSL, and the same two wavelet-based detection methods: *mr_filter* (Starck & Pierre 1998) and *PGWave* (Damiani et al. 1997; Ciprini et al. 2007). The methods looked for sources on top of the diffuse emission model described in § 3. For *mr_filter* the threshold was set in each image using the False Discovery Rate procedure (Benjamini & Hochberg 1995) at 5% of false detections. For *PGWave* we used a flat threshold at 4 σ. For comparison with the BSL, the number of 'seed' sources from *mr_filter* was 857 in the full band, 932 in the medium band and 331 in the hard band. Contrary to the BSL procedure, we combined the results of those two methods (eliminating duplicates) rather than choosing a baseline method and using the other for comparison. The rationale was to limit the number of missed sources to a minimum, since the later steps do not introduce any additional sources. Duplicates were defined after the first localization (*pointfit* in § 4.2, run separately on each list of seeds). If two resulting positions were consistent within the quadratic sum of 95% error radii only one source was kept (that with highest significance estimate). Where *pointfit* did not converge the 95% error radius was set to 0.3°, typical for faint sources (§ 4.2).

To that same end we also introduced for 1FGL two other detection methods:

- *pointfind*, a tool that searches for candidate point sources by maximizing the likelihood function for trial point sources at each direction in a HEALPix order 9 (pixel size ∼0.1 deg^2) tessellation of the sky. The algorithm for evaluating the likelihood is optimized for speed by using energy-dependent binning of the photon data, choosing 4 energy bands per decade starting at 700 MeV, and a HEALPix order commensurate with the PSF width in each band. A first pass examines the significance of a trial point source at the center of each pixel, on the assumption that the diffuse background is adequately described by the model for Galactic diffuse emission and ignoring any nearby point sources. The likelihood is optimized with respect to the signal fraction (i.e., the source and diffuse intensities are not fit separately) in each energy band, with the total likelihood being the product over all the bands. This makes the result

independent of the spectrum of the point source or of the diffuse background. While the search is quite efficient, it produces many false signals, so a second pass is used to optimize a more detailed likelihood function which includes nearby detected sources and fits the test source flux and diffuse background normalization independently. The result of this pass is a map of Test Statistic from which the coordinates of candidate point sources can be derived.

- the minimum spanning tree (Campana et al. 2008) looks for clusters of high- energy events (> 4 GeV outside the Galactic plane and > 10 GeV at $|b| < 15°$). It is restricted to high energies because it does not account for structured background, but can efficiently detect very hard sources.

We combined the 'seed' positions from those two methods with those from the wavelet-based methods, using the same procedure for removing duplicates as above.

Finally, we introduced external seeds from the BZCAT (Massaro et al. 2009) and WMAP (Wright et al. 2009) catalogs. In order to not bias the 1FGL catalog toward those external sources, we used them as seeds only when there was no seed from the detection methods within its 95% error radius. Of the 335 BZCAT seeds introduced, 24 survived as LAT gamma-ray sources in this catalog. Of the 7 WMAP seeds, 3 remain in the catalog.

The variety of seeds that we used means that the catalog is not homogeneous. Because of the strong underlying diffuse emission, achieving a truly homogeneous catalog was not possible in any case. What we aimed at here is provide enough seeds so that the main defining step of the catalog is the main maximum likelihood analysis (§ 4.3). The total number of seeds was 2433.

4.2. Localization

The localization of faint or soft sources is more sensitive to the diffuse emission and to nearby sources than for brighter sources, so we proceeded in three steps instead of just one for the bright sources considered in the BSL:

1. The first step consisted of localizing the sources before the main maximum likelihood analysis (§ 4.3) as we did for the BSL (using *pointfit*), treating each source independently but in descending order of significance and incorporating the bright sources into the background for the fainter ones. This is fast and a good enough starting point for step 2.

2. The second step consisted of improving the localization within the main maximum likelihood analysis (§ 4.3) using the *gtfindsrc* utility in the Science Tools[3]. Again sources are considered in descending order of significance. When localizing one source, the others are fixed in position, but the flux and spectral index of sources within 2° are left free, allowing to compensate lost low energy photons in the model if the source that is being localized moves away. At the end of that step we have a good representation of the location, flux and spectral shape of the sources over the entire sky, but a single error radius to describe the error box.

3. The third step is new and described in more detail below. It uses a similar framework as the first step, but incorporates the results of the main maximum likelihood analysis for all sources other than the one being considered, so it has a good representation of the source's surroundings. It is faster than *gtfindsrc* and *gttsmap* and returns a full Test Statistic map around each source and an elliptical representation as well as an indicator of the quality of the elliptical fit.

The first and third steps used a likelihood analysis tool (*pointfit*) that provides speed at little sacrifice of precision by maximizing a specially-constructed binned likelihood function. Photons are assigned to energy bands (four per decade from 100 MeV to 100 GeV) and HEALpix-based spatial bins for which the size is selected to be small compared with the scale set by the PSF. Since the PSF for *Front*-converting photons is significantly smaller than that for *Back* conversions, there are separate spatial bins for *Front* and *Back*. Note that the width of the PSF at a given energy is only a weak function of incidence angle. For *pointfit* the likelihood function is evaluated using the PSF averaged over the full field of view for each energy band. For each band, we define the likelihood as a function of the position and flux of the assumed point source, and adopt as the background the sum of Galactic diffuse, isotropic diffuse (see § 3) and any nearby (i.e., within 5°), other point sources in the catalog. The flux for each band is then evaluated by maximizing the likelihood of the data given the model. using the coordinates defined by *gtfindsrc*. The overall likelihood function, as a function of the source position, is then the product of the band likelihoods. We define a function of the position $\mathbf{p}$, as $2(\log(L_{\max}) - \log(L(\mathbf{p})))$, where L is the likelihood function described above. This function, according to Wilks' theorem (Wilks 1938), is the probability distribution for the coordinates of the point source consistent with the observed data. Note that the width of this distribution is a measure of the uncertainty, and that it scales directly with the width of the PSF.

---

[3]Available from the *Fermi* Science Support Center, http://fermi.gsfc.nasa.gov/ssc.

We then fit the distribution to a 2-dimensional quadratic form with 5 parameters describing the expected elliptical shape: the coordinates (R.A. and Dec.) of the center of the ellipse, semi-major and -minor axis extents (θ_1 and θ_2), and the position angle ϕ of the ellipse. A 'quality' factor is evaluated to represent the goodness of the fit: it is the square root of the sum of the squares of the deviations for 8 points sampled along the contour where the value is expected to be 4.0, that is, 2 σ from the maximum likelihood coordinates of the source.

We quote the parameters of the ellipse that would contain 95% of the probability: for Gaussian errors that is a radius of 2.45 σ. The result of an analysis of the deviations of 396 AGNs at high latitudes from the positions of the nearest LAT point sources indicated that the PSF width is underestimated, on average, by a factor of 1.10 ± 0.05. Thus the final uncertainties reported by *pointfit* were scaled up by a factor of 1.1. To visually assess the fits, a Test Statistic map was made for each source, and these were considered in evaluating the analysis flags that are discussed in § 4.8.

Twelve sources did not converge at the third step, converged to a point far away ($> 1°$) or were in crowded regions where the procedure (which does not have free parameters for the fluxes of nearby sources) may not be reliable. Those 12 were left at their *gtfindsrc* positions. They can be easily identified in the 1FGL catalog because they have identical semimajor and semiminor axes for the source location uncertainty, and position angle 0. The LAT-detected pulsars and X-ray binaries, which were placed at their true positions, have null values in the localization parameters.

Figure 2 illustrates the resulting position errors as a function of the Test Statistic (TS) values obtained in § 4.3. The relatively large dispersion that is seen at a given TS is in part due to the different local conditions (level of diffuse γ-ray emission) but primarily to the source spectrum. Hard sources are better localized than soft ones for the same TS (Fig. 3) because the PSF is so much narrower at high energy. At our threshold of $TS = 25$ the typical 95% position error is about $10'$, and most 95% errors are below $20'$.

4.3. Significance and thresholding

The detection and localization steps provide estimates of significance, but not very accurate ones. The detection step does not explicitly use the energy information and the localization fits one source at a time. To better estimate the source significances we use a 3-dimensional maximum likelihood algorithm (*gtlike*) in unbinned mode (i.e., the position and energy of each event is considered individually) applied on the full energy range from
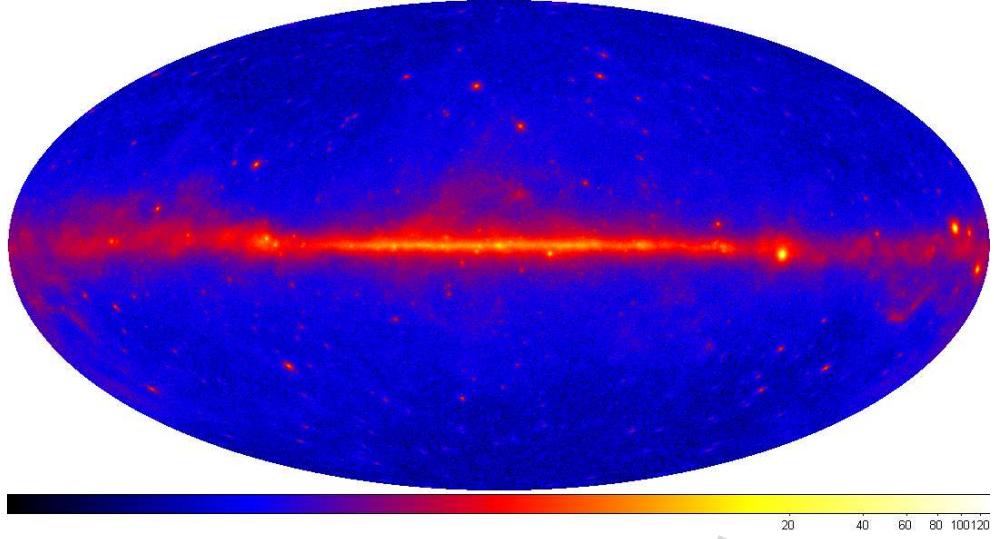
Fig. 1.— Sky map of the LAT data for the time range analyzed in this paper, Aitoff projection in Galactic coordinates. The image shows γ-ray intensity for energies >300 MeV, in units of photons m^{-2} s^{-1} sr^{-1}.
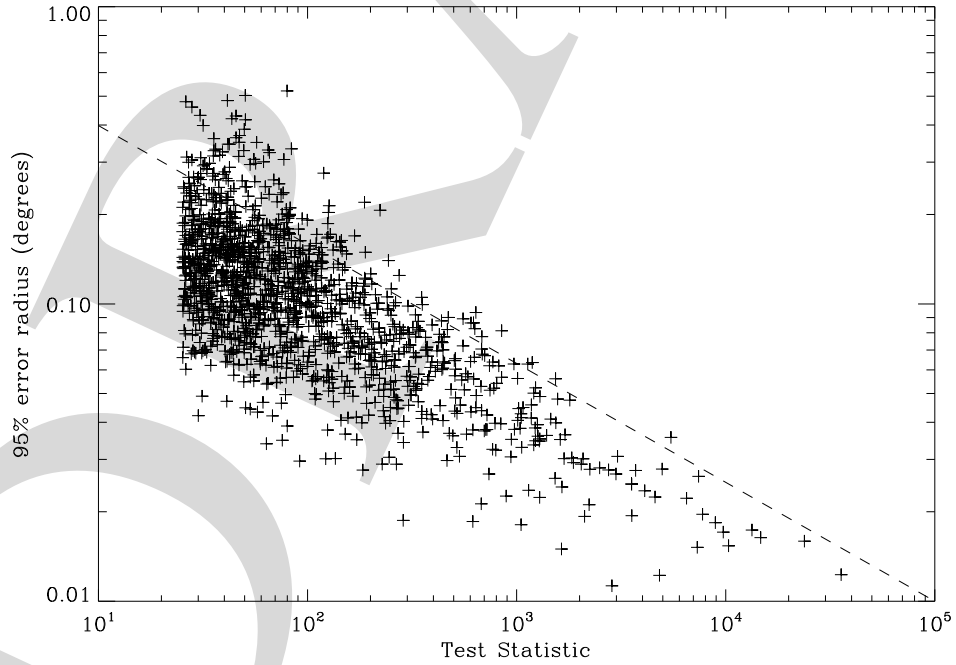

Fig. 2.— 95% source location error (geometric mean of the two axes of the ellipse) as a function of Test Statistic (§ 4.3). The dotted line is a $TS^{-0.4}$ trend for reference (not adjusted vertically).
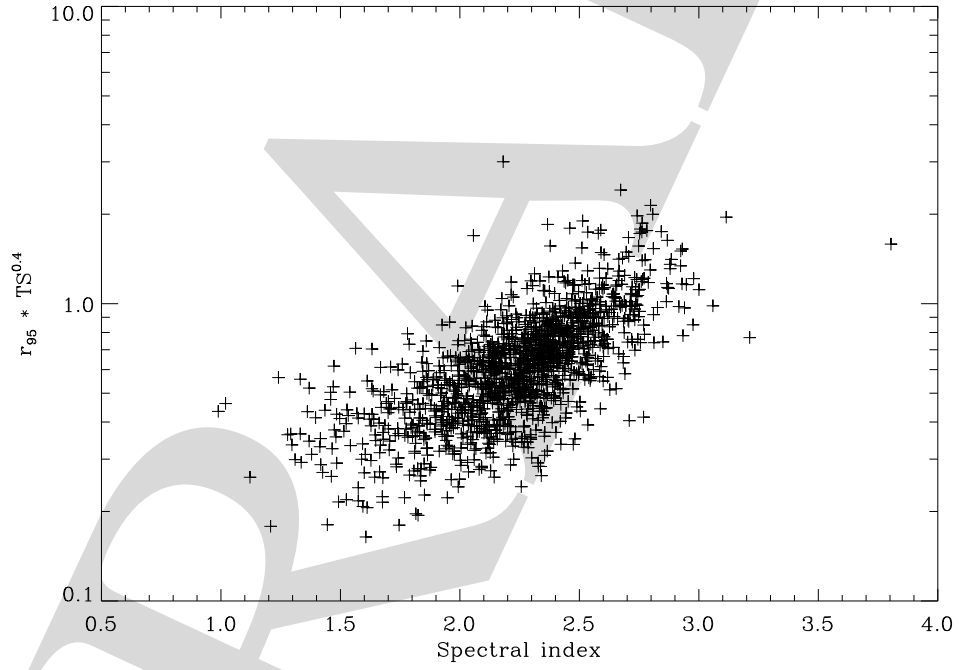
Fig. 3.— 95% source location error multiplied by $TS^{0.4}$ to remove the global trend (Figure 2) as a function of the photon spectral index from § 4.3.

100 MeV to 100 GeV. This is part of the standard Science Tools software package[4] currently at version 9r15p5. That tool does not vary the source position, but does adjust the source spectrum. It should be noted that *gtlike* does not include the energy dispersion in the TS calculation (i.e., it assumes that the measured energy is the true energy). Given the 8 to 10% energy resolution of the LAT over the wide energy bands used in the present analyses, this approximation is justified. The underlying optimization engine is Minuit[5]. The code works well with up to ~30 free parameters, an important consideration for regions where sources are close enough together to partially overlap. The *gtlike* tool provides for each source the best-fit parameters and the Test Statistic $TS = 2\Delta\log$(likelihood) between models with and without the source. Error estimates (and a full covariance matrix) are obtained from Minuit in the quadratic approximation around the best fit. For this stage we modeled the sources with simple power-law spectra.

Because the fitted fluxes and spectra of the sources can be very sensitive to even slight errors in the spectral shape of the diffuse emission we allow the Galactic diffuse model (§ 3) to be corrected (i.e., multiplied) locally by a power law in energy with free normalization and spectral slope. The slope varies between 0 and 0.07 (making it harder) in the Galactic plane and the normalization by ± 10% (down from 0.15 and 20% for the BSL). The smaller excursions of that corrective slope when compared to the BSL reflect the better fit of the current diffuse model to the data. The normalization of the isotropic component of the diffuse emission (which represents the extragalactic and residual backgrounds) was left free. The three free parameters were separately adjusted in each Region of Interest (see below).

The TS associated with each source is a measure of the source significance, or equivalently the probability that such an excess can be obtained from background fluctuations alone. The probability distribution in such a situation (source over background) is not known precisely (Protassov et al. 2002). However since we consider only positive fluctuations, and each fit involves four degrees of freedom (two for position, plus flux and spectral index), the probability to get at least TS at a given position in the sky is close to 1/2 of the χ^2 distribution with four degrees of freedom (Mattox et al. 1997), so that $TS = 25$ corresponds to a false detection probability of 2.5×10^{-5} or 4.1 σ (one sided). For the BSL we considered only two degrees of freedom because the localization was based on a simpler algorithm which did not involve explicit minimization of the same quantity.

The sources that we see are best (most strongly) detected around 1 GeV. This is approximately the median of the Pivot_Energy quantity in the catalog, i.e., the energy at which the

---

[4]http://fermi.gsfc.nasa.gov/ssc/data/analysis/documentation/Cicerone/

[5]http://lcgapp.cern.ch/project/cls/work-packages/mathlibs/minuit/doc/doc.html

uncertainties in normalization and spectral index for the power-law fit are uncorrelated. At 1 GeV the 68% containment radius is approximately $r_{68} = 0.8°$. The number of independent elements in the sky (trials factor) is about $4\pi/(\pi r_{68}^2)$ in which r_{68} is converted to radians. This is about 2×10^4 so at a threshold of $TS = 25$ we expect less than 1 spurious source by chance only. If any, there might be a few very hard spurious sources in the catalog because hard sources have a smaller effective PSF so that the trials factor is larger. The main reason for potentially spurious sources, though, is our imperfect knowledge of the underlying diffuse emission (§ 4.6).

We split the sky into overlapping circular Regions of Interest (RoI). The source parameters are free in the central part of each RoI (RoI radius $- 7°$) such that all free sources are well within the RoI even at low energy (7° is larger than r_{68} at 100 MeV). It is advantageous (for the global convergence over the entire sky) to use large RoIs, but we limit the RoI size so that not more than 8 sources are free at a time. Adding 3 parameters for the diffuse model, the total number of free parameters in each RoI is normally 19 at most. We needed 445 RoIs to cover the 2433 seed positions. The RoI radii range between 9° and 15°.

We proceed iteratively. All RoIs are processed in parallel and a global current model is assembled after each step in which the best fit parameters for each source are taken from the RoI whose center is closest to the source. The local model for one RoI includes sources up to 7° outside the RoI (which can contribute at low energy due to the broad PSF). Their parameters are fixed to their values in the global model at the previous step. The parameters of the sources inside the RoI but closer than 7° to the border are also fixed except in two cases (this was not done for the BSL):

- Sources within 2° of any source inside the central part because they can influence that inner source. 2° is chosen to be larger than twice the containment radius at 1 GeV $(2 \times 0.8°)$ where the LAT sensitivity peaks (Figure 4). We leave both flux and spectral index free for those.

- Very bright sources contributing more than 5% of the total counts in the RoI because they can influence the diffuse emission parameters. We leave only the flux free for those.

All seed sources start at 0 flux at the first step (the starting point for the slope is 2). We iterate over 5 steps (the fits change very little after the fourth). To facilitate the convergence the seed sources are not entered all at once. The 10% brightest are entered at the first step, 30% at the second step, and finally all at the third step. At each step we remove seed sources with low TS, raising the threshold for inclusion into the global model from 10 at the third step to 15 at the fourth and finally 25 at the last step. All seeds are reentered at

the fourth step to avoid losing faint sources before the global model has fully converged. We have checked on simulations that removing the faint sources has little impact on the bright ones, much less than changing the diffuse model (§ 4.6). This procedure left 1451 sources above threshold.

One can obtain an approximate but reasonably accurate estimate of the detection threshold for a point source at any point in the sky, assuming that the diffuse background is locally uniform and considering only one source. In that approximation, one may replace the sum over event probabilities in the likelihood function by an integral over the expected spatial $\mathrm{PSF}(\theta, E)$ (θ is the angular distance between the source location and the event direction) and spectral $S_S(E)$ source distribution on top of the background spectrum $S_B(E)$ per unit solid angle. We again neglect the energy redistribution and to simplify the algebra we consider the limit in which the source counts are small with respect to the background counts over the entire RoI. Introducing the equivalent on-axis observing time T_0, the effective area $A_{\mathrm{eff}}(E)$, and the local source to background ratio $g(\theta, E) = S_S(E)\mathrm{PSF}(\theta, E)/S_B(E)$ one gets

$$TS = 2T_0 \int_{E_{\min}}^{E_{\max}} A_{\mathrm{eff}}(E)\, dE \left(\int_0^\pi (S_S(E)\mathrm{PSF}(\theta, E) + S_B(E)) \log(1 + g(\theta, E))\, d\Omega - S_S(E) \right) \quad (1)$$

$$TS = T_0 \int_{\log E_{\min}}^{\log E_{\max}} W(E)\, d\log E \quad (2)$$

$$W(E) = 2E A_{\mathrm{eff}}(E) S_B(E) \int_0^\pi (1 + g(\theta, E)) \log(1 + g(\theta, E)) - g(\theta, E)\, d\Omega \quad (3)$$

Here $W(E)$ is the contribution to TS per unit log(energy). It is illustrated on Figure 4 (dashed line) for a power-law source spectrum. At low energy (below 1 GeV) faint sources are always background limited, i.e., $g(\theta, E)$ is small even at $\theta = 0$. In that limit, the dominant term of the integrand in the integral over θ in Eq. 3 is $g(\theta, E)^2/2$. Noting that $\int_0^\pi \mathrm{PSF}(\theta, E)^2 d\Omega = C_{\mathrm{sh}}(E)\sigma(E)^{-2}$ in which $\sigma(E)$ is the angular resolution and $C_{\mathrm{sh}}(E)$ is a shape factor weakly dependent on energy, one gets

$$W(E) = E C_{\mathrm{sh}}(E) \frac{A_{\mathrm{eff}}(E) S_S(E)^2}{S_B(E)\sigma(E)^2} \quad (4)$$

This explicitly shows that the weight is proportional to the ratio of source counts over background counts within the angular resolution. The strong PSF improvement with energy (approximately as $E^{-0.8}$) means that for a $E^{-2.2}$ source (which is not far from the background spectral shape) $W(E) \propto A_{\mathrm{eff}}(E)E^{0.4}$. Since $A_{\mathrm{eff}}(E)$ improves with energy up to 1 GeV, this explains the rising part of $W(E)$. At high energy (above several GeV) the PSF is good enough that even the faint sources are limited by their own count rate ($g(0, E) > 1$) and Eq. 4 no longer applies. When the source density is large, a first-order way to account for
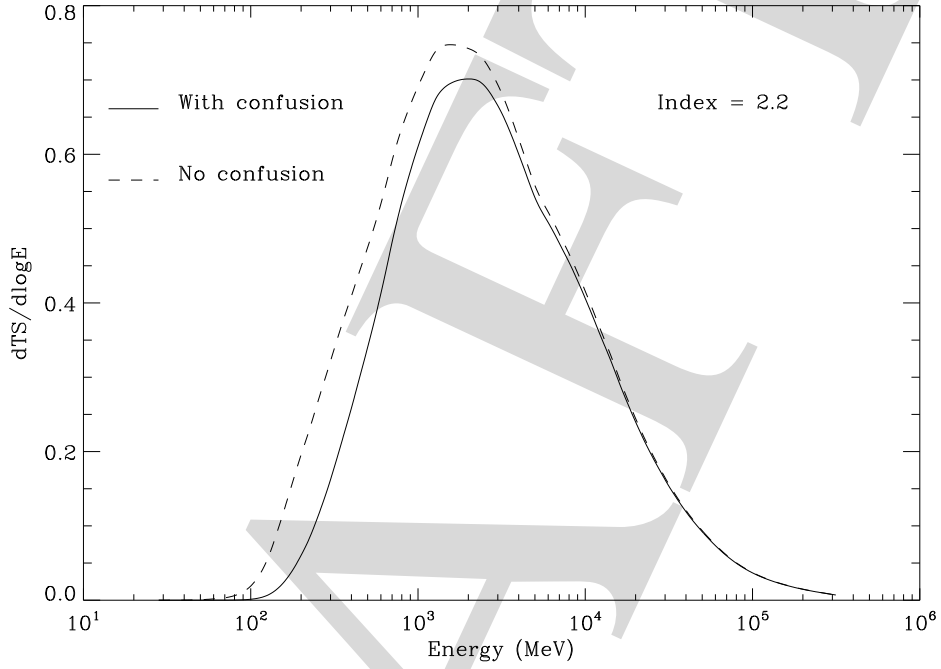
Fig. 4.— Theoretical contribution ($W(E)$ of Eq. 3) to Test Statistic per Ms and per $\log(E)$ interval as a function of energy for a power-law source over the average background at $|b| > 10°$. The assumed photon spectral index is 2.2. The dashed line is for an isolated source. The full line includes approximately the effect of source confusion.
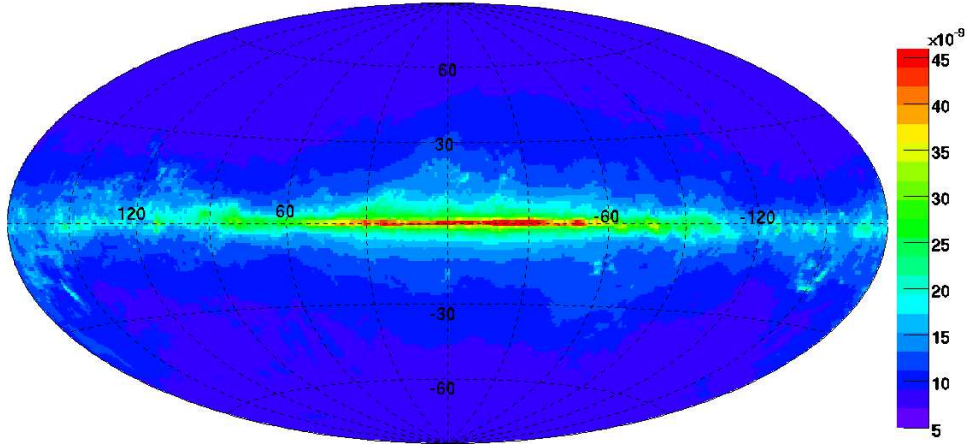
Fig. 5.— Flux (E>100 MeV in ph cm^{-2} s^{-1}) needed to reach $TS = 25$ in the LAT data for the 11-month time range considered in this paper, as a function of position in Galactic coordinates. The assumed photon spectral index is 2.2.

Fig. 6.— Photon flux above 100 MeV of sources at $|b| > 10°$ as a function of spectral index. The dashed line shows the theoretical detection threshold at $TS = 25$ for an isolated source over the average extragalactic background. The full line includes approximately the effect of source confusion as on Figure 4.

confusion is to limit the integral over angles in Eq. 3 to $\theta_{\max}$ such that $\pi\theta_{\max}^2 = \Omega_{\mathrm{tot}}/N_{\mathrm{src}}$ is the averag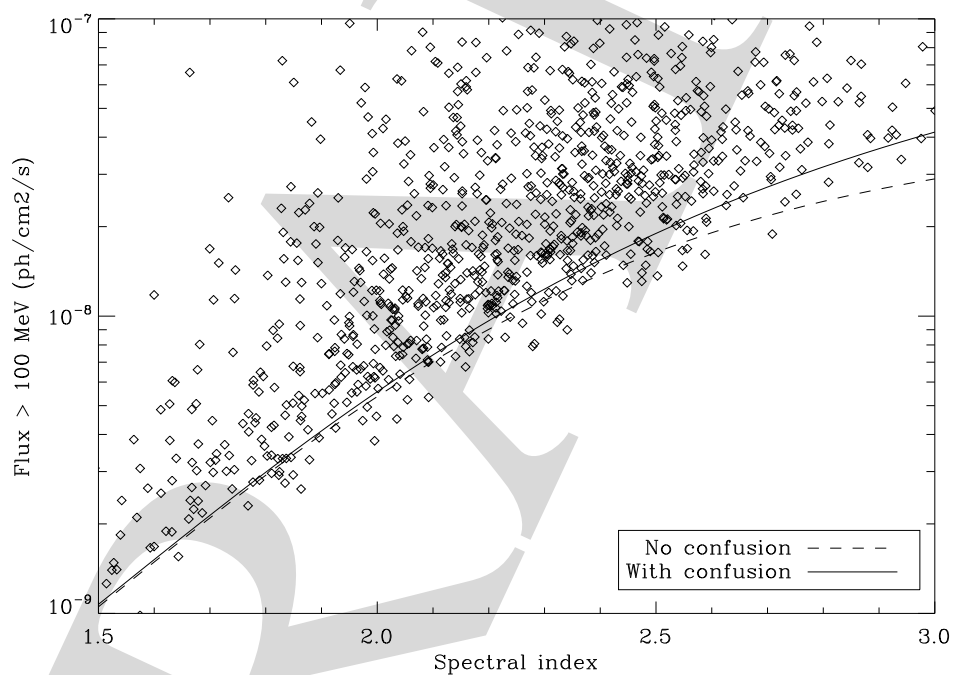e solid angle per source. This is shown by the solid line on Figure 4. The effect is of course larger where the PSF is broader, at low energy.

Setting $TS = 25$ in Eq. 1, assuming a given source spectral shape and solving for the normalization of the source spectrum provides the detection threshold. The spatial dependence of that threshold is shown on Figure 5. The Galactic diffuse and isotropic backgrounds are taken from the model (§ 3). T_0 is computed at each point using the pointing history during the 11 months, and the source spectrum is assumed to be $E^{-2.2}$, the average spectral slope of the sources. Although the nonuniform exposure affects this map somewhat, the dominant factor is the strong diffuse emission along the Galactic plane. Because of the strong energy dependence of the PSF, the detection threshold depends very sensitively on the spectral index as well. Figure 6 illustrates that, in terms of the photon flux above 100 MeV, it ranges from 10^{-9} to 4×10^{-8} ph cm^{-2} s^{-1} going from very hard sources ($\Gamma = 1.5$) to soft ones ($\Gamma = 3$). It uses the same recipe for confusion as in Figure 4. A few sources are below the line. This can happen for purely statistical reasons, and because the background and exposure depend a little on direction even after taking out the Galactic plane.

4.4. Flux Determination

The maximum likelihood method described in § 4.3 provides good estimates of the source significances and the overall spectral slope, but not very accurate estimates of the fluxes. This is because the spectra of most sources do not follow a single power law over that broad an energy range (three decades). Among the two most populous categories, the AGN often show a broken power-law spectrum and the pulsars an exponentially cut off one. In both cases fitting a single power law over the entire range overshoots at low energy where most of the photons are, and therefore biases the fluxes high. On the other hand the effect on the significance is low due to the broad PSF and high background at low energies.

In addition, the significance is mostly based on GeV photons (Figure 4) whereas the photon flux in the full range (above 100 MeV) is dominated by lower energy events so that the uncertainty on that flux can be quite large even for quite significant sources. For example, the typical relative uncertainty on the photon flux above 100 MeV is 23% for a $TS = 100$ source with spectral index 2.2.

To provide better estimates of the source fluxes, we have decided to split the range in five energy bands from 100 to 300 MeV, 300 MeV to 1 GeV, 1 to 3 GeV, 3 to 10 GeV and 10 to 100 GeV. (There aren't enough counts to justify two bands in the last decade.) The list

of sources remains the same in all bands of course. It is impossible to fit the spectral index in each of those relatively narrow energy bands (and the flux estimate does not depend very much on the index), so we simply froze the spectral index of each source to the best fit over the full interval. The spectral bias to the Galactic diffuse emission (§ 4.3) was also frozen.

The estimate from the sum of the five bands is on average within 30% of the flux obtained in the previous section, with excursions up to a factor 2. We have also compared those estimates with a more precise spectral model for the three bright pulsars (Vela, Geminga and the Crab). The sum of the five fluxes is within 5% of the more precise flux estimate, whereas the power-law estimate is 25% too high for Vela and Geminga. However because it is not based on extrapolating a relatively well defined power-law fit the relative uncertainty on that flux is even larger than that on the power-law fit, typically 50% for a $TS = 100$ source with spectral index 2.2. For that reason we do not show that very poorly measured quantity in Table 3. We provide instead the photon flux between 1 and 100 GeV (the sum of the three high energy bands), which is much better defined. The relative uncertainty on that flux is typically 18% for a $TS = 100$ source with spectral index 2.2.

On the other hand, the energy flux over the full band is better defined than the photon flux because it does not depend as much on the poorly-measured low-energy fluxes. So we provide this quantity in Table 3. Here again the sum of the energy fluxes in the five bands provides a more reliable estimate of the overall flux than the power-law fit. The relative uncertainty on the energy flux between 100 MeV and 100 GeV is typically 26% for a $TS = 100$ source with spectral index 2.2.

An additional difficulty that does not exist when considering the full data is that, because we wish to provide the fluxes in all bands for all sources, we must handle the case of sources that are not significant in one of the bands. Many sources have $TS < 10$ in one or several bands: 1135 in the 100 to 300 MeV band, 630 in the 300 MeV to 1 GeV band, 359 in the 1 to 3 GeV band, 503 in the 3 to 10 GeV band and 800 in the 10 to 100 GeV band. It is particularly difficult to measure fluxes below 300 MeV because of the large source confusion and the modest effective area of the LAT at those energies with the current event cuts (§ 2). For the sources with poorly-measured fluxes (where $TS < 10$ or the nominal uncertainty is larger than half the flux itself), we replace the flux value from the likelihood analysis by a $2\,\sigma$ upper limit, indicating the upper limit by a 0 in the flux uncertainty column of Table 7. The upper limit is obtained by looking for $2\Delta\log(\text{likelihood}) = 4$ when increasing the flux from the best fit). When the best fit is very close to 0 (i.e., the true best fit would be at negative flux), solving $2\Delta\log(\text{likelihood}) = 4$ tends to underestimate the upper limit. Whenever $TS < 1$ we switch to the Bayesian method proposed by Helene (1983). We do not use that method throughout because it is about five times slower.

The five fluxes provide a rough spectrum, allowing departures from a power law to be judged. This is the main advantage over the BSL scheme which involved only two bands. Examples of those rough spectra are given in Figures 7 and 8 for a bright pulsar (Vela) and a bright blazar (3C 454.3). In order to quantify departures from a power-law shape, we introduce a Curvature_Index

$$C = \sum_i \frac{(F_i - F_i^{\mathrm{PL}})^2}{\sigma_i^2 + (f_i^{\mathrm{rel}} F_i)^2} \tag{5}$$

where i runs over all bands and F_i^{PL} is the flux predicted in that band from the power-law fit. f_i^{rel} reflects the relative systematic uncertainty on effective area described in § 4.6. It is set to 10, 5, 10, 15 and 20% in the bands [0.1,0.3], [0.3,1], [1,3], [3,10] and [10,100] GeV respectively. Note that this systematic uncertainty on the effective area is not included in the uncertainties reported in Table **??**, because comparing one source to another in the same band does not suffer from this.

We use for F_i and σ_i the true best fit and 1-sigma estimates even when the values are reported as upper limits in the table, both for computing the Curvature_Index and the sums (photon flux and energy flux). In a number of cases the photon flux or energy flux have nominal uncertainty larger than half the flux itself. We report those cases as upper limits from the sum of the flux estimate plus twice the uncertainty. They occur because the Test Statistic (Eq. 1) does not depend on the data in the same way as the flux measurements. There are also a number of sources which have upper limits in all bands, even though they are formally significant (as defined in § 4.3) over the entire band.

As shown by diffuse (Abdo et al. 2009e) and source (Abdo et al. 2009f, 2010d) observations, the LAT data produce spectra systematically steeper than those reported in EGRET analysis. LAT fluxes are greater at energies below 200 MeV and less at energies above a few GeV.

Since the power-law fit involves two parameters (normalization and spectral index), C would be expected to follow a χ^2 distribution with $5 - 2 = 3$ degrees of freedom if the power-law hypothesis was true. At the 1% confidence level, the spectral shape is significantly different from a power-law if $C > 11.34$. That condition is met by 225 sources (at 1% confidence, we expect 15 false positives). The curvature index is by no means an estimate of curvature itself, just a statistical indicator. A faint source with a strongly curved spectrum can have the same curvature index as a bright source with a slightly curved spectrum. Since the relative uncertainties on the fluxes in each band are quite different and depend on the spectral index itself, it is difficult to build a curvature indicator similar to the fractional variability for the light curves. It is also not specific to curvature. Any kind of deviation from the best fit power-law can trigger that index, although curvature is by far the most
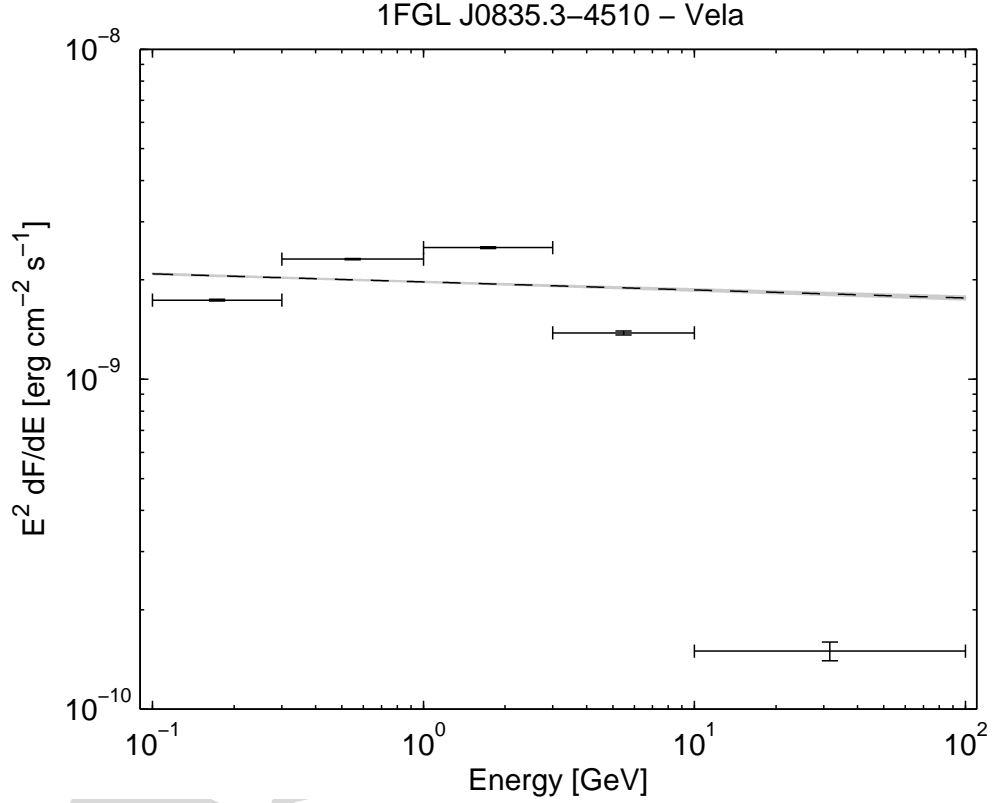
Fig. 7.— Sample spectrum of Vela (1FGL J0835.3−4510) generated from the five energy-band flux measurements in the catalog and plotted as $E_i^2 \Delta F_i / \Delta E_i$, with E_i chosen to be the center of the energy bin in log space. The energy range of the integration is indicated by a horizontal bar. The vertical bar indicates the statistical error on the flux. The point at which these bars cross is not the same as the differential power per unit log bandwidth, $E^2 dF/dE$ at E_i. The dashed lines (nearly coincident for this very bright source) reflect the uncertainties on the flux and index of the power-law fit to the full energy range in § 4.3.

Fig. 8.— Spectrum of the bright blazar 3C 454.3 (1FGL J2253.9+1608).

common.

4.5. Variability

Variability is very common in γ-rays (particularly among accreting sources) and it is useful to estimate it. To that end we use the same energy range as in § 4.3 (100 MeV to 100 GeV). To avoid ending up with too large error bars in relatively short time intervals, we froze the spectral index of each source to the best fit over 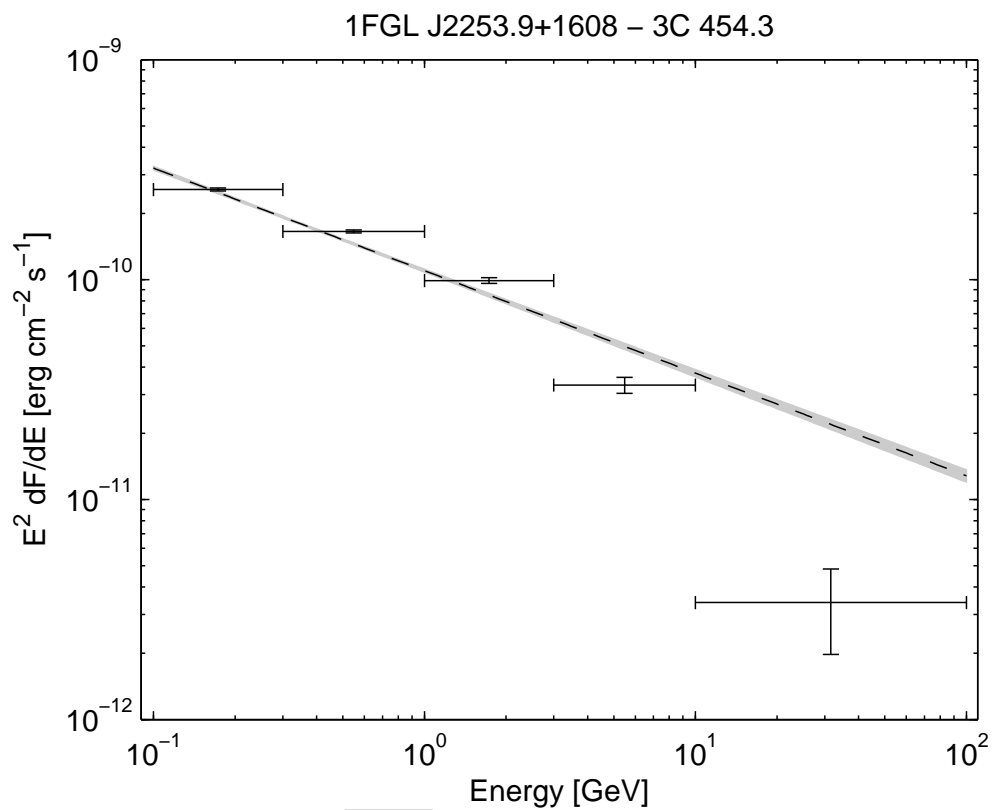the full interval. Sources do vary in spectral shape as well as in flux, of course, but we do not aim at characterizing source variability here, just detecting it. It is very unlikely that a true variability in shape will be such that it will not show up in flux at all. In addition, little spectral variability was found in bright AGN where it would be detectable if present (Abdo et al. 2010h).

We split the full 11-month interval into $N_{\mathrm{int}} = 11$ intervals of about one month each (2624 ks or 30.37 days). This is much more than the week used in the BSL, in order to preserve some statistical precision for the majority of faint sources we are dealing with here. It is also far enough from half the precession period of the orbit ($\approx 0.5 \times 53.4 = 26.7 days$) that we do not expect possible systematic effects as a function of off-axis angle to be coherent with those intervals. Because we do not expect the diffuse emission to vary, we freeze the spectral adjustment of the Galactic diffuse component to the local (in the same RoI) best fit over the full interval. So the fitting procedure is the same as in § 4.4 with all spectral shape parameters frozen.

As in § 4.4 it often happens that a source is not significant in all intervals. To preserve the variability index (Eq. 6) we keep the best fit value and its estimated error even when the source is not significant. This does not work, however, when the best fit is close to zero because in that case the log(likelihood) as a function of flux is very asymmetric. Whenever $TS < 10$ or the nominal uncertainty is larger than half the flux itself we compute the 2 σ upper limit and replace the error estimate with half the difference between that upper limit and the best fit. This is an estimate of the error on the positive side only. Because the log(likelihood) profile often gets below the parabolic extrapolation at 2 σ this is more conservative than computing the 1 σ upper limit directly. The best fit itself is retained. Note that this error estimate can be a large overestimate of the error on the negative side, particularly in the deep Poisson regime at high energy. This explains why σ_i/F_i can be as high as 1 even when TS is 4 or so in that interval. As in § 4.4 we switch to the Bayesian method whenever $TS < 1$.

Examples of light curves are given in Figures 9 and 10 for a bright constant source
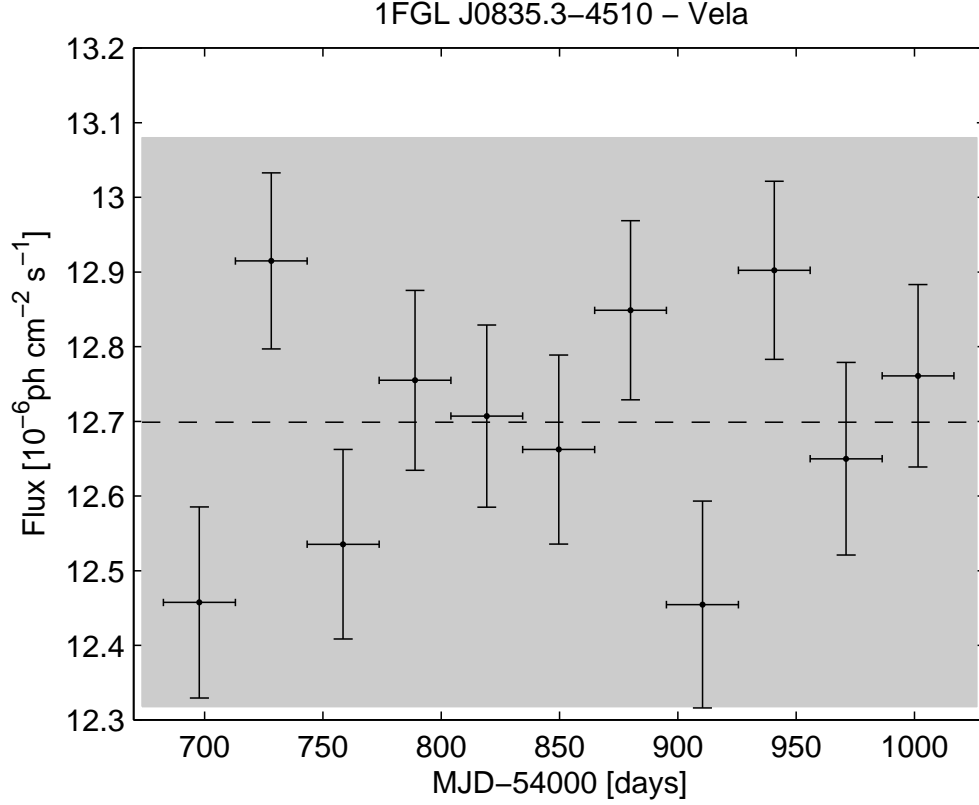
Fig. 9.— Light curve of Vela (1FGL J0835.3−4510) for the 11-month interval analyzed for the Catalog. The fluxes are integrated from 100 MeV to 100 GeV using single power-law fits and the error bars indicate the 1 σ statistical errors. The grey band shows the conservative 3% systematic error that we have adopted for evaluating the variability index. Vela is not seen to be variable even at the level of the statistical uncertainty. The spectrum of Vela is not well described by a power law and the fluxes shown here overestimate the true flux, but the overestimate does not depend on time.

1FGL J2253.9+1608 – 3C 454.3

Fig. 10.— Light curve of 3C 454.3 (1FGL J2253.9+1608), which exhibits extreme variability. The grey band is the same 3% systematic uncertainty that we have adopted for evaluating the variability index.

(the Vela pulsar) and a bright variable source (the blazar 3C 454.3). As for the BSL we have added in quadrature a fraction $f_{rel} = 3\%$ of the flux for each interval F_i to the error estimates in the Unc_Flux_History column (for each 1-month time interval) used to compute the variability index. With that systematic relative uncertainty no pulsar is found variable. The very brightest pulsars (Vela and Geminga) appear to have observed variability below 3% (this is apparent in Figure 9, so this may be overly conservative. It is not a critical parameter though, as it affects only the very bright sources.

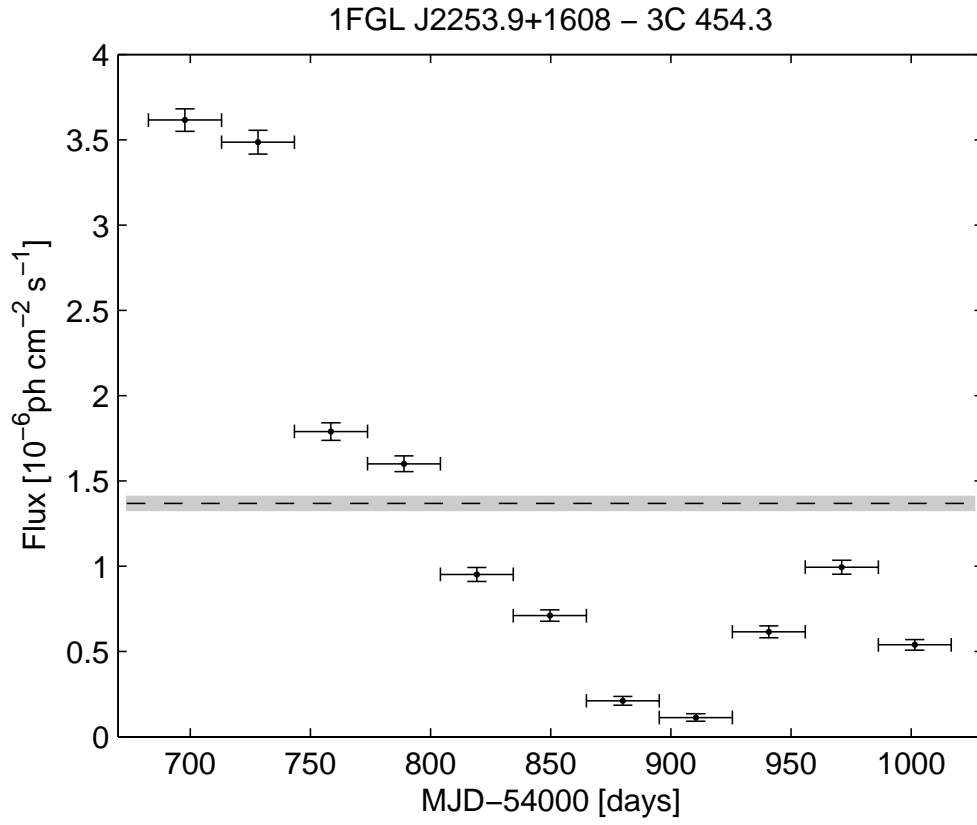The variability index is defined as a simple χ^2 criterion:

$$V = \sum_i \frac{(F_i - F_{av})^2}{\sigma_i^2 + (f_{rel} F_i)^2} \tag{6}$$

where i runs over the 11 intervals and σ_i is the statistical uncertainty in F_i. Since F_{av} is not known a priori, this parameter is expected, in the absence of variability, to follow a χ^2 distribution with 10 ($= N_{int} - 1$) degrees of freedom. At the 1% confidence level, the light curve is significantly different from a flat one if $V > 23.21$. That condition is met by 242 sources (at 1% confidence, we expect 15 false positives). For those sources we provide directly in the table the maximum monthly flux (Peak_Flux) and its uncertainty, as well as the time when it occurred (Time_Peak).

The fractional variability of the sources is defined from the excess variance on top of the statistical and systematic fluctuations:

$$\delta F / F = \sqrt{\frac{\sum_i (F_i - F_{av})^2}{(N_{int} - 1) F_{av}^2} - \frac{\sum_i \sigma_i^2}{N_{int} F_{av}^2} - f_{rel}^2} \tag{7}$$

The typical fractional variability is 50%, with only a few strongly variable sources beyond $\delta F / F = 1$. This is qualitatively similar to what was reported on Figure 8 of Abdo et al. (2009k). The criterion we use is not sensitive to relative variations smaller than 60% at $TS = 100$. That limit goes down to 20% as TS increases to 1000. We are certainly missing many variable AGN below $TS = 100$ and up to $TS = 1000$. There is no indication that fainter sources are less variable than brighter ones, but we simply cannot measure their variability.

Both the curvature index and the variability index are pointing at certain types of sources. This is best illustrated on Figure 11 plotting one against the other for the main types of sources (from the association procedure described in § 6). One can clearly separate the pulsar branch at large curvature and small variability from the blazar branch at large variability and smaller curvature.
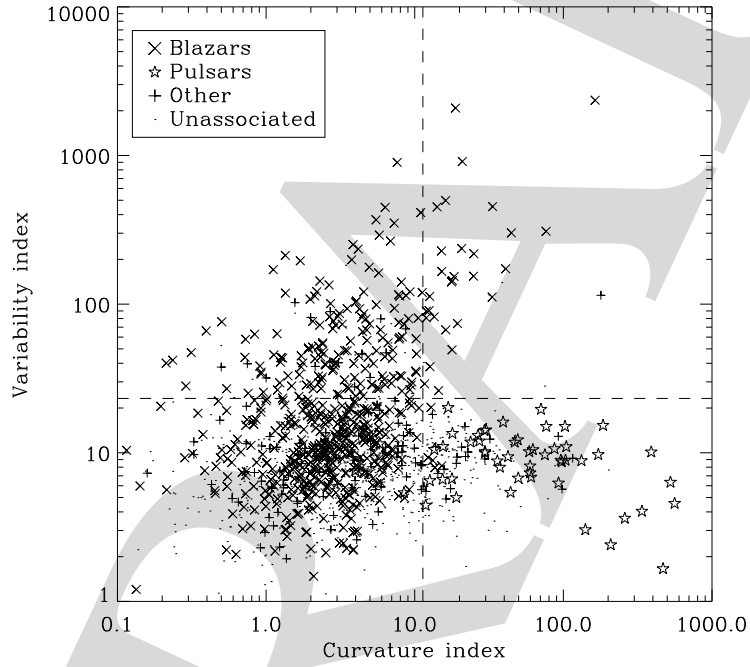
Fig. 11.— Variability index plotted as a function of curvature index (§ 4.4). The horizontal dashed line shows where we set the variable source limit. The vertical dashed line shows where the spectra start deviating from a power-law. Pulsars are shown as stars, AGN as + signs, other associations as diamonds, unassociated sources as dots.

4.6. Limitations and Systematic Uncertainties

A limitation of this work is that we did not attempt to test for source extension. All sources are assumed to be point-like. This is true for the major source populations in the GeV range (blazars, pulsars). On the other hand the TeV instruments have detected many extended sources in the Galactic plane, mostly pulsar wind nebulae and supernova remnants, (e.g. Aharonian et al. 2005) and the LAT has already started detecting extended sources (e.g. Abdo et al. 2009g). Because measuring extension over a PSF which varies so much with energy is delicate,we are not yet ready to address this matter systematically across all the sources in a large catalog such as this.

We have addressed the issue of systematics for localization in § 4.2. But another related limitation is confusion. This is of course strong in the inner Galaxy (§ 4.7) but it is also a significant issue elsewhere. The average distance between sources outside the Galactic plane is $3°$ in 1FGL, to be compared with a per photon containment radius $r_{68} = 0.8°$ at 1 GeV where the sensitivity is best. The ratio between both numbers is not large enough that confusion can be neglected. The simplest way to quantify this is to look at the distribution of distances between each source and its nearest neighbor (D_n) in the area of the sky where the source density is uniform, i.e., outside the Galactic plane. This is shown in Figure 12. The source concentration in the Galactic plane is very narrow (less than $1°$) but we need to make sure that those sources do not get chosen as nearest neighbors so we select $|b| > 10°$. The histogram of D_n (after taking out the geometric factor as in Figure 12) should follow

$$H(D_n) = N_{\text{true}} \, \rho_{\text{src}} \, \exp\left(-\pi D_n^2 \rho_{\text{src}}\right) \tag{8}$$

where ρ_{src} is the source density (number of sources per square degree) and N_{true} is the true number of sources (after correcting for missed sources due to confusion). The exponential term is the probability that no nearest source exists. It is apparent that, contrary to expectations, the histogram dips toward 0. This indicates that confusion is important, even in the extragalactic sky. The effect disappears only at distances larger than $1.5°$. To get N_{true}, one may solve for the number of observed sources at distances beyond $1.5°$. Since $\rho_{\text{src}} = N_{\text{true}}/A_{\text{tot}}$ in which A_{tot} is the sky area at $|b| > 10°$, this amounts to solving

$$N_{\text{obs}}(> 1.5°) = N_{\text{true}} \, \exp\left(-N_{\text{true}} A_0/A_{\text{tot}}\right) \tag{9}$$

in which A_0 is the area up to $1.5°$. This results in $N_{\text{true}} - N_{\text{obs}} = 80$ missed sources on top of the $N_{\text{obs}} = 1043$ sources observed at $|b| > 10°$. Those missed sources are probably the reason for some of the asymmetries in the TS maps discussed in § 4.2. The conclusion is that globally we missed nearly 10% of the extragalactic sources. But because of the worse PSF at low energy soft sources are comparatively more affected than hard sources. This is approximately indicated by the difference between the full and the dashed lines on Figure 6.

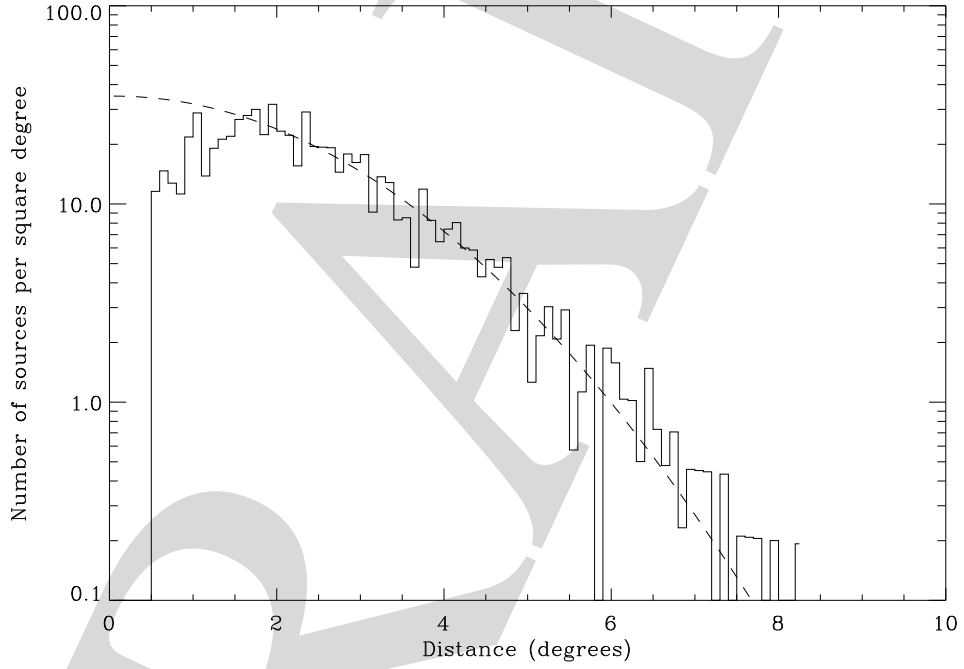Fig. 12.— Distribution of the distance D_n to the nearest neighbor of all detected sources at $|b| > 10°$. The number of entries is divided by $2\pi D_n \Delta D_n$ in which ΔD_n is the distance bin, in order to eliminate the 2-dimensional geometry. The overlaid curve is the expected gaussian distribution for a uniform distribution of sources with no confusion (Eq. 8 normalized using Eq. 9).

The next important issue is the systematic uncertainties on the effective area of the instrument. At the time of the BSL we used pre-launch calibration and cautioned that there were indications that our effective area was reduced in flight due to pile-up. Since then, the pile-up effect has been integrated in the simulation of the instrument Rando et al. (2009) and many tests have shown that the resulting calibration (P6_V3) is consistent. The estimate of the remaining systematic uncertainty is 10% at 100 MeV, 5% at 500 MeV rising to 20% at 10 GeV and above. This uncertainty applies uniformly to all sources. Our relative errors (comparing one source to another or the same source as a function of time) are much smaller, as indicated in § 4.5. The fluxes resulting from that calibration are systematically higher than the BSL fluxes. For example, the flux of the three brightest pulsars (Vela, Geminga and Crab) is about 30% larger in 1FGL than in the BSL. The difference is more pronounced for soft sources than hard ones. This implies also that the 1FGL fluxes are significantly larger than the EGRET fluxes in the 3EG catalog (Hartman et al. 1999) which happened to be close to the BSL fluxes.

The diffuse emission is the other important source of uncertainties. Contrary to the former, it does not affect all sources equally. It is smaller outside the Galactic plane ($|b| > 10°$) where the diffuse emission is faint and varying on large angular scales. It is also less of a worry in the high bands (> 3 GeV) where the PSF is sharp enough that the sources dominate the background under the PSF. But it is a serious issue inside the Galactic plane ($|b| < 10°$) in the low bands (< 1 GeV) and particularly inside the Galactic ridge ($|l| < 60°$) where the diffuse emission is strongest and very structured, following the molecular cloud distribution. It is not easy to assess precisely how large the uncertainty is, for lack of a proper reference. We discuss the Galactic ridge more specifically in § 4.7. For an automatic assessment we have tried re-extracting the source fluxes assuming a different diffuse model, derived from GALPROP (as we did for the BSL) but with protons and electrons adjusted to the data (globally). The model reference is 54_87Xexph7S. The results show that the systematic uncertainty more or less follows the statistical one (i.e., it is larger for fainter sources) and is of the same order. More precisely, the dispersion is 0.7 σ on flux and 0.5 σ on spectral index at $|b| > 10°$, and 1.8 σ on flux and 1.2 σ on spectral index at $|b| < 10°$. We have not increased the errors accordingly, though, because this alternative model does not fit the data as well as the reference model. From that point of view we may expect this estimate to be an upper limit. On the other hand both models rely on nearly the same set of H I and CO maps of the gas in the interstellar medium, which we know are an imperfect representation of the mass. That is, some systematic uncertainties are not accounted for by the comparison. So we present the figures as qualitative estimates.

4.7. Sources Toward Local Interstellar Clouds and the Galactic Ridge

Figure 13 shows an example of the striking, and physically unlikely, correspondence between the 1FGL sources and tracers of the column density of interstellar gas, in this case E(B–V) reddening. The sources in Orion are tightly associated with the regions with greatest column densities. No particular gamma-ray sources are known to be associated with the cloud complex. Even if radio quiet pulsars were the sources, they would not be expected to be aligned so closely with the regions of highest column densities. The implication is that peak column densities are being systematically underestimated in the the model for the Galactic diffuse emission used in the analysis. E(B–V) is not directly used in the model; as described in § 3 the column densities are derived from surveys of H I and CO line emission, the latter as a tracer of molecular hydrogen. An E(B–V) 'residual' map E(B–V)$_{res}$, representing interstellar reddening that his not correlated with N(H I) or W(CO), is included in the model. So the peak column densities would need to be underestimated both in CO and E(B–V). We are studying the effect and strategies for validating the model for Galactic diffuse emission at high column densities.

Figure 13 illustrates a second, better understood issue with the model for Galactic diffuse emission. In the Orion nebula (near $l, b \sim 209°$, $-19.5°$), a massive star-forming region that is extremely bright in the infrared, the infrared color corrections used to evaluate E(B–V) are inaccurate and the column densities inferred from E(B–V) are underestimated; the depression in E(B–V) in the nebula does not correspond to a decreased column density of gas. The model of Galactic diffuse emission was constructed with E(B–V)$_{res}$ allowed to be a signed correction for the column densities inferred from H I and CO lines. This made essential improvements in large regions, allowing errors in the assumed spin temperature of H I to be corrected in the total column densities, but in discrete directions toward massive star-forming regions, negative E(B–V)$_{res}$ can introduce deep depressions in the predicted diffuse emission. Figure 14 illustrates the depression around the S225 star-forming region, and its close correspondence with a 1FGL source.

Similar considerations relate to the sources at low latitudes in the inner Galaxy. The density of unassociated sources in the Galactic ridge ($300° < l < 60°, |b| < 1°$) is very high, and their latitude distribution is very narrow (Fig. 15. If they are true gamma-ray emitting sources they must have a very small scale height in the Milky Way, like young massive star-forming regions traced by ultracompact H II regions ($\sim 25'$ FWHM, e.g., Giveon et al. 2005) or be quite distant and hence very luminous. The inferred luminosities of these sources would be unreasonably high if the scale height of their distribution is characteristic of most Pop I tracers. In addition to the concerns about the accuracy of column densities toward the peaks of interstellar clouds, self absorption of H I at low latitudes can introduce small-scale
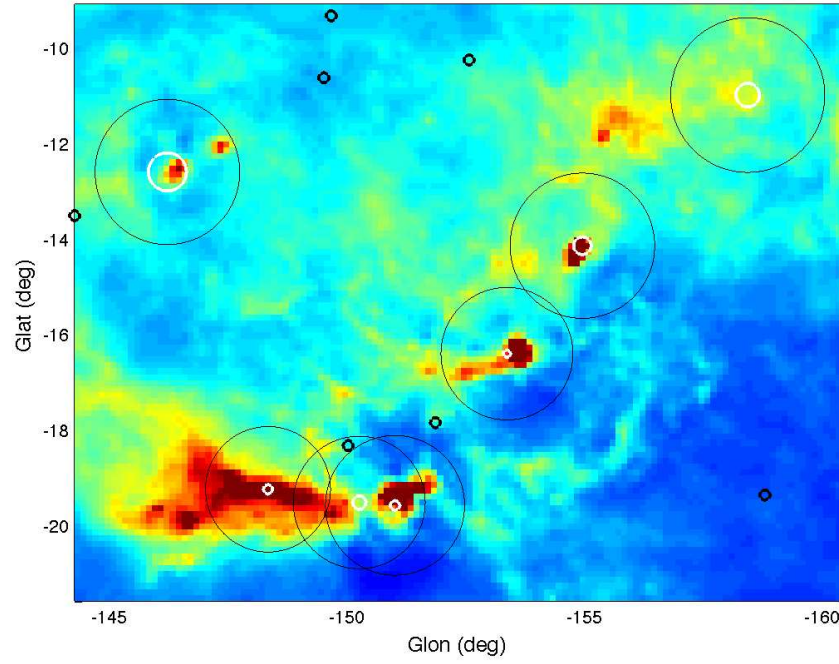
Fig. 13.— Overlay of 1FGL sources on color scale representation of E(B–V) reddening in Orion (Schlegel et al. 1998). The small circles indicate the positions and 95% confidence regions for the 1FGL sources in the field. The larger circles indicate the effective (spectrally-weighted) 68% containments for events associated with each source; these can be considered to represent the region of the sky most relevant for the definition of each source.
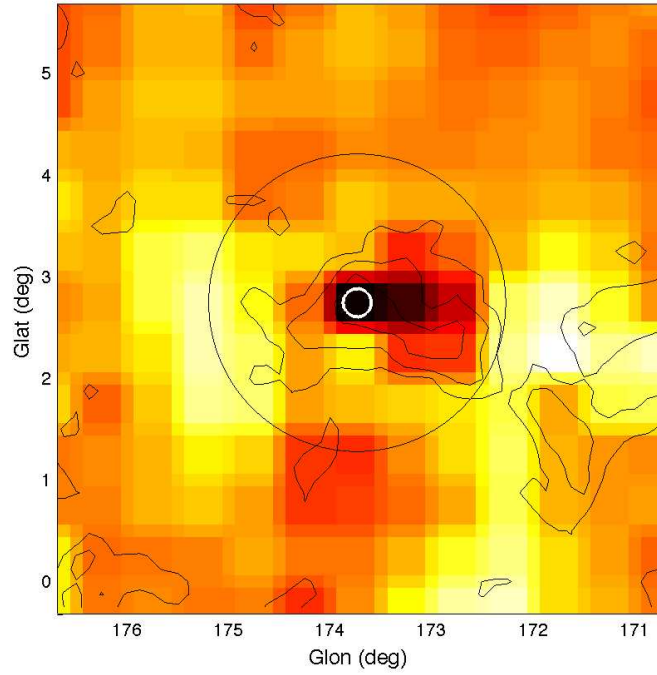
Fig. 14.— Overlay of 1FGL J0541.1+3542 on color scale representation of E(B–V)$_{res}$ residual interstellar reddening in the S225 H II region. The small circle indicates the position and 95% confidence region for the 1FGL source in the field. The larger circle indicates the effective (spectrally-weighted) 68% containment for events associated with each source. The contours are W(CO), tracing column density of molecular gas.

underestimates of the column densities, and intensities of the diffuse emission.

The 1FGL sources toward the peaks of local interstellar clouds and the Galactic ridge all have analysis flags set (§ 4.8) in the Catalog. **We have also added a designator 'c' to their names to indicate that they are to be considered as potentially confused with interstellar diffuse emission or perhaps spurious.** In addition, the 'c' designator is used for 1FGL sources in regions of high density outside the Galactic ridge, as a caution about the complications of regions where the PSFs overlap.

4.8. Analysis Flags

We have identified a number of conditions that can shed doubt on a source. They are described in Table 2. As noted, setting of flags 4 and 5 depends on the energy band. High energy is always more favorable for source detection and characterization because the PSF is narrower there, and often sources have harder spectra than the diffuse background, so the flags are set on the basis of the highest band in which a source is significant. Flag 5 signals confusion and depends on a reference distance $\theta_{\rm ref}$. Because statistics are better at low energy (enough events to sample the core of the PSF), $\theta_{\rm ref}$ is set to the Full Width at Half Maximum (FWHM) there (minimum distance to have two peaks with a local mimimum in between in the counts map). At high energy there are fewer events so $\theta_{\rm ref}$ is set to the larger value $2r_{68}$. In the intermediate bands we interpolate between FWHM and $2r_{68}$. In the FITS version of the Catalog, these flags are summarized in a single integer column (Flags). Each condition is indicated by one bit among the 16 bits forming Flags. The bit is raised (set to 1) in the dubious case, so that good sources have Flags = 0.

5. The 1FGL Catalog

In this section we tabulate the quantities listed in Table 3 for each source; see Table 4 for descriptions of the columns. The source designation is `1FGL JHHMM.m+DDMM` where the `1` refers to this being the first LAT catalog, `FGL` represents *Fermi* Gamma-ray LAT. Sources close to the Galactic ridge and some nearby interstellar cloud complexes are assigned names of the form `1FGL JHHMM.m+DDMMc`, where the `c` indicates that caution should be used in interpreting or analyzing these sources. Errors in the model of interstellar diffuse emission, or an unusually high density of sources, are suspected to affect the measured properties or even existence of these sources (see § 4.7).

The integrated photon flux for 1–100 GeV (F_{35}) and the energy flux for 100 MeV to
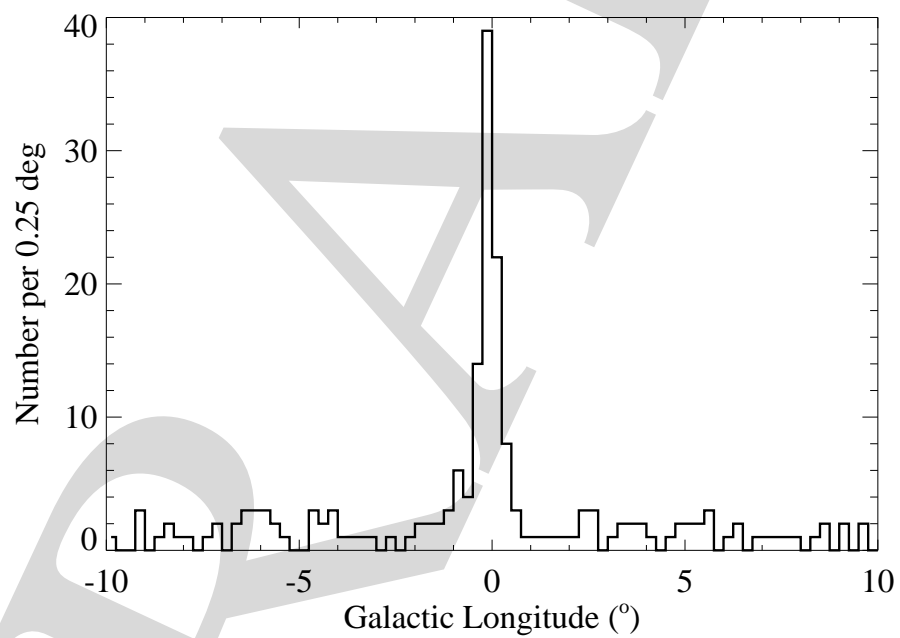
Fig. 15.— Latitude distribution of unassociated/unidentified 1FGL sources in the Galactic ridge ($|l| < 60°$).

Table 2.   Definitions of the Analysis Flags

Flag[a]	Meaning
1	Source with $TS > 35$ which went to $TS < 25$ when changing the diffuse model (§ 4.6). Note that sources with $TS < 35$ are not flagged with this bit because normal statistical fluctuations can push them to $TS < 25$.
2	Moved beyond its 95% error ellipse when changing the diffuse model.
3	Flux or spectral index changed by more than $3\,\sigma$ when changing the diffuse model. Requires also that the flux change by more than 35% (to not flag strong sources).
4	Source-to-background ratio less than 30% in highest band in which $TS > 25$. Background is integrated over πr_{68}^2 or 1 square degree, whichever is smaller .
5	Closer than $\theta_{\rm ref}$ from a brighter neighbor. $\theta_{\rm ref}$ is defined in highest band in which source $TS > 25$. $\theta_{\rm ref}$ is set to 2.6° (FWHM) below 300 MeV, 1.52° between 300 MeV and 1 GeV. 0.84° between 1 GeV and 3 GeV and $2\,r_{68}$ above 3 GeV.
6	On top of an interstellar gas clump or small-scale defect in the model of diffuse emission.
7	Unstable position determination; result from *gtfindsrc* outside the 95% ellipse from *pointlike* (see § 4.2).
8	*pointlike* did not converge. Position from *gtfindsrc.*
9	Elliptical quality > 10 in *pointlike* (i.e., TS contour does not look elliptical).

[a]In the FITS version the values are encoded in a single column, with Flag n having value $2^{(n-1)}$. For information about the FITS version of the table see Table 4 and § 5.

100 GeV in Table 3 are evaluated from the fluxes in bands presented in Table 7. The energy fluxes in each band are derived on the assumption that the spectral shape is the same as for the overall power-law fit (Γ_{25}). This is an approximation but the bands are narrow enough that the energy fluxes are not strongly dependent on the spectral index. We do not present the integrated photon flux for 100 MeV to 100 GeV because the relative uncertainties tend to be very large, because of the limited effective area. Figure 16 shows the distribution of integrated fluxes (1 GeV – 100 GeV) for all of the sources in the catalog. The dynamic range is approximately 2.5 orders of magnitude, owing both to the intrinsic range of fluxes of the gamma-ray sources as well as their spectral hardnesses.

Table 3.   1FGL Catalog

Name 1FGL	R.A.	Decl.	l	b	θ_1	θ_2	ϕ	σ	F_{35}	ΔF_{35}	S_{25}	ΔS_{25}	Γ_{25}	$\Delta\Gamma_{25}$	Curv.	Var.	Flags	γ-ray Assoc.	Class	ID or Assoc.	Ref.
J0000.8+6600c	0.209	66.002	117.812	3.635	0.112	0.092	−73	9.8	2.9	0.6	35.2	5.7	2.60	0.09	⋯	⋯	6	⋯	⋯	⋯	⋯
J0000.9−0745	0.236	−7.763	88.903	−67.237	0.179	0.130	16	5.6	1.0	0.0	9.2	3.0	2.41	0.20	⋯	⋯	⋯	⋯	bzb	CRATES J0001−0746	⋯
J0001.9−4158	0.482	−41.982	334.023	−72.028	0.121	0.116	53	5.5	0.5	0.2	14.4	0.0	1.92	0.25	⋯	⋯	⋯	⋯	⋯	⋯	⋯
J0003.1+6227	0.798	62.459	117.388	0.108	0.119	0.112	−19	7.8	2.1	0.5	19.9	4.9	2.53	0.10	T	⋯	3	⋯	⋯	⋯	⋯
J0004.3+2207	1.081	22.123	108.757	−39.448	0.183	0.157	58	4.7	0.6	0.2	5.3	2.5	2.35	0.21	⋯	⋯	⋯	⋯	⋯	⋯	⋯
J0004.7−4737	1.187	−47.625	323.864	−67.562	0.158	0.148	−5	6.6	0.8	0.3	10.9	3.3	2.56	0.17	⋯	⋯	⋯	⋯	bzq	PKS 0002−478	⋯
J0005.1+6829	1.283	68.488	118.689	5.999	0.443	0.307	−4	6.1	1.4	0.5	17.0	4.8	2.58	0.12	⋯	⋯	1,4	⋯	⋯	⋯	⋯
J0005.7+3815	1.436	38.259	113.151	−23.743	0.216	0.186	32	8.4	0.6	0.3	13.6	3.1	2.86	0.13	⋯	⋯	⋯	⋯	bzq	B2 0003+38A	⋯
J0006.9+4652	1.746	46.882	115.082	−15.311	0.194	0.124	32	10.2	1.1	0.3	18.3	3.4	2.55	0.11	⋯	⋯	⋯	⋯	⋯	⋯	⋯
J0007.0+7303	1.757	73.052	119.660	10.463	⋯	⋯	⋯	119.7	63.4	1.5	432.5	10.1	1.97	0.01	T	⋯	⋯	0FGL J0007.4+7303 EGR J0008+7308 1AGL J0006+7311	PSR	LAT PSR J0007+7303	1,2,3
J0008.3+1452	2.084	14.882	107.655	−46.708	0.144	0.142	−42	4.7	0.8	0.2	9.6	0.0	2.00	0.21	⋯	⋯	⋯	⋯	⋯	⋯	⋯
J0008.9+0635	2.233	6.587	104.426	−54.751	0.120	0.114	65	5.0	0.8	0.0	6.1	3.0	2.28	0.22	⋯	⋯	⋯	⋯	bzb	CRATES J0009+0628	⋯
J0009.1+5031	2.289	50.520	116.089	−11.789	0.119	0.108	72	8.5	1.3	0.3	15.6	3.4	2.41	0.13	⋯	⋯	⋯	⋯	⋯	⋯	⋯

References. — 1 Abdo et al. (2008), 2 Abdo et al. (2009n), 3 Abdo et al. (2009a)

Note. — Photon flux units for F_{35} are 10^{-9} cm^{-2} s^{-1}; energy flux units for S_{25} are 10^{-12} erg cm^{-2} s^{-1}. The designator FRBA in the Associations column is used for blazars detected with VLA observations as part of the 'Finding (and Rejecting) Blazar Associations for Fermi-LAT Sources' observing program. These are described in Abdo et al. (2010, The First Catalog of Active Galactic Nuclei Detected by the Fermi Large Area Telescope, ApJS submitted). This table is published in its entirety in the electronic edition of the Astrophysical Journal Supplements. A portion is shown here for guidance regarding its form and content.

Table 4.   LAT First Catalog Description

Column	Description
Name	1FGL JHHMM.m+DDMM[c], constructed according to IAU Specifications for Nomenclature; m is decimal minutes of R.A.; in the name R.A. and Decl. are truncated at 0.1 decimal minutes and 1′, respectively; c indicates that based on the region of the sky the source is considered to be potentially confused with Galactic diffuse emission
R.A.	Right Ascension, J2000, deg, 3 decimal places
Decl.	Declination, J2000, deg, 3 decimal places
l	Galactic Longitude, deg, 3 decimal places
b	Galactic Latitude, deg, 3 decimal places
θ_1	Semimajor radius of 95% confidence region, deg, 3 decimal places
θ_2	Semiminor radius of 95% confidence region, deg, 3 decimal places
ϕ	Position angle of 95% confidence region, deg. East of North, 0 decimal places
σ	Significance derived from likelihood Test Statistic for 100 MeV–100 GeV analysis, 1 decimal place
F_{35}	Photon flux for 1 GeV–100 GeV, 10^{-9} ph cm^{-2} s^{-1}, summed over 3 bands, 1 decimal place
ΔF_{35}	1-σ uncertainty on F_{35} , same units and precision
S_{25}	Energy flux for 100 MeV–100 GeV, 10^{-12} erg cm^{-2} s^{-1}, from power-law fit, 1 decimal place
ΔS_{25}	1-σ uncertainty on S_{25}, same units and precision
Γ	Photon number power-law index, 100 MeV–100 GeV, 2 decimal places
$\Delta\Gamma$	1 σ uncertainty of photon number power-law index, 100 MeV–100 GeV, 2 decimal places
Curv.	T indicates < 1% chance that the power-law spectrum is a good fit to the 5-band fluxes; see note in text
Var.	T indicates < 1% chance of being a steady source; see note in text
Flag	See Table 1 for definitions of the flag numbers
γ-ray Assoc.	Positional associations with 0FGL, 3EG, EGR, or AGILE sources
Class	Like 'ID' in 3EG catalog, but with more detail (see Table 5). Capital letters indicate firm identifications; lower-case letters indicate associations.
ID or Assoc.	Designator of identified or associated source
Ref.	Reference to associated paper(s)

Table 5.   LAT First Catalog Source Classes

Class	Description
PSR	pulsar, identified by pulsations
pwn	pulsar wind nebula
glc	globular cluster
snr	supernova remnant
mqo	micro-quasar object = X-ray binary (black hole or neutron star) with radio jet
xrb	other X-ray binary
bzb	BL Lac type of blazar
bzq	FSRQ type of blazar
agn	other non-blazar agn
agu	active galaxy of uncertain type
gal	normal galaxy
sbg	starburst galaxy
†	Special case - potential association with SNR or PWN (see Table 2)

Note. — Designations shown in capital letters are firm identifications; lower case letters indicate associations. In the case of AGN, many of the associations have high confidence (Abdo et al. 2010i). Among the pulsars, those with names beginning with LAT are newly discovered by the LAT.

Table 6.   Potential Associations for Sources Near SNRs (PRELIMINARY)

Name 1FGL	l	b	Assoc.
J0218.8+6158	133.01	0.82	SNR G132.7+01.3
J0220.0+6257	132.80	1.80	SNR G132.7+01.3
J0500.1+5237	155.63	6.34	SNR G156.2+05.7
J0503.2+4526	161.64	2.35	SNR G160.9+02.6
J0538.6+2717	180.59	−2.16	SNR G180.0−01.7
J0553.9+3105	179.08	2.65	SNR G179.0+02.6
J0636.0+0458	206.74	−1.15	SNR G205.5+00.5
J0823.3−4248	260.37	−3.15	SNR G260.4−03.4
J0841.9−4620	265.18	−2.58	SNR G263.9−03.3
J0854.0−4632	266.64	−1.09	SNR G266.2−01.2 (Vela Junior)
J1018.6−5856	284.32	−1.70	SNR G284.3−01.8 (MSH 10−53), PSR J1013−5915
J1119.4−6127	292.17	−0.52	SNR G292.2−00.5, PSR J1119−6127, PWN G292.2−0.5
J1134.8−6055	293.77	0.57	SNR G293.8+00.6, PWN G293.8+0.6
J1213.7−6240	298.63	−0.12	SNR G298.6−00.0
J1343.7−6239	308.89	−0.39	SNR G308.8−00.1
J1350.8−6212	309.80	−0.12	SNR G309.8+00.0
J1410.3−6128	312.21	−0.03	SNR G312.4−00.4, PSR J1410−6132
J1442.0−6000	316.34	−0.05	SNR G316.3−00.0
J1501.6−4204	327.30	14.55	SNR G327.6+14.6
J1513.2−5904	320.28	−1.07	SNR G320.4−01.2
J1514.7−5917	320.33	−1.35	SNR G320.4−01.2
J1521.8−5734	322.03	−0.38	SNR G321.9−00.3
J1552.4−5609	326.25	−1.71	SNR G326.3−01.8, PWN G326.3−1.8
J1617.5−5105	332.39	−0.40	SNR G332.4−00.4
J1640.8−4634	338.29	−0.06	SNR G338.3−00.0, PWN G338.3−0.0
J1711.7−3944	347.15	−0.19	SNR G347.3−00.5
J1725.5−2832	357.96	3.91	SNR G358.0+03.8
J1745.6−2900	359.94	−0.05	SNR G000.0+00.0, PWN G359.95−0.04
J1801.3−2322	6.57	−0.22	SNR G006.4−00.1 (W28)
J1805.2−2137	8.55	−0.14	SNR G008.7−00.1 (W30)
J1806.8−2109	9.13	−0.24	SNR G008.7−00.1 (W30)
J1826.2−1450	16.88	−1.29	SNR G016.8−01.1
J1834.3−0842	23.24	−0.20	SNR G023.3−00.3 (W41)
J1834.7−0709	24.67	0.43	SNR G024.7+00.6
J1916.0+1110	45.67	−0.31	SNR G045.7−00.4
J2020.0+4049	78.37	2.53	SNR G078.2+02.1
J2042.3+5041	88.66	5.19	SNR G089.0+04.7

The procedure used to designate associated sources and class designations is described in § 6.2. Figure 17 shows the distribution of the 1FGL sources on the sky by source class, and Figure 18 shows just the inner Galaxy. Figure **??** shows the distribution of sources with significant spectral curvature.

Figure 19 selects just the variable sources, i.e., those with $<1\%$ chance of being steady sources in the monthly light curves and those with spectra incompatible with power laws. The variable sources are seen to be predominantly outside the Galactic plane, and many are associated with blazars. The spectrally-curved sources have a distribution much more confined to the Galactic equator.

The electronic version of the 1FGL catalog, available from the *Fermi* Science Support Center, includes all of the information in these tables plus the monthly light curves from which the variability index values were derived and pivot energies for the overall power-law fits; see Table 8.

Table 6—Continued

Name 1FGL	l	b	Assoc.
J2046.0+4954	88.42	4.24	SNR G089.0+04.7
J2046.4+3041	73.40	−7.79	SNR G074.0−08.5
J2049.1+3142	74.56	−7.60	SNR G074.0−08.5
J2055.2+3144	75.40	−8.59	SNR G074.0−08.5
J2057.4+3057	75.11	−9.46	SNR G074.0−08.5

Note. — See text. These sources are marked with a † in Table X. They may be pulsars rather than the SNR or PWN named.

Table 7. First LAT Catalog: Spectral Information

				100 MeV – 300 MeV			300 MeV – 1 GeV			1 GeV – 3 GeV			3 GeV – 10 GeV			10 GeV – 100 GeV		
Name 1FGL	Γ	$\Delta\Gamma$	Curv.	F_1[a]	ΔF_1[a]	$\sqrt{TS_1}$	F_2[a]	ΔF_2[a]	$\sqrt{TS_2}$	F_3[b]	ΔF_3[b]	$\sqrt{TS_3}$	F_4[c]	ΔF_4[c]	$\sqrt{TS_4}$	F_5[c]	ΔF_5[c]	$\sqrt{TS_5}$
J0000.8+6600c	2.60	0.09	⋯	8.3	0.0	2.6	1.9	0.3	6.4	2.6	0.6	5.2	3.7	1.5	4.1	0.8	0.0	0.0
J0000.9−0745	2.41	0.20	⋯	2.9	0.0	2.5	0.5	0.0	3.0	0.7	0.0	2.2	3.8	0.0	3.7	1.5	0.0	2.4
J0001.9−4158	1.92	0.25	⋯	2.1	0.0	1.8	0.2	0.0	1.1	0.6	0.0	2.2	2.9	1.1	6.0	1.7	0.0	0.0
J0003.1+6227	2.53	0.10	T	3.0	0.0	0.0	1.7	0.3	6.8	2.0	0.5	5.0	4.3	0.0	1.4	1.4	0.0	1.9
J0004.3+2207	2.35	0.21	⋯	1.8	0.0	0.9	0.4	0.0	1.8	0.4	0.2	3.2	1.9	0.9	3.8	0.9	0.0	0.0
J0004.7−4737	2.56	0.17	⋯	2.4	0.8	3.3	0.3	0.1	3.6	0.8	0.2	5.0	2.0	0.0	2.0	1.5	0.0	0.2
J0005.1+6829	2.58	0.12	⋯	3.9	0.0	0.6	1.3	0.3	5.3	2.2	0.0	3.1	4.9	0.0	2.0	1.0	0.0	0.0
J0005.7+3815	2.86	0.13	⋯	3.3	0.9	3.7	0.5	0.1	4.4	1.1	0.0	3.1	2.5	0.0	1.6	1.1	0.0	0.0
J0006.9+4652	2.55	0.11	⋯	2.9	0.9	3.3	0.7	0.1	6.4	0.8	0.3	3.7	3.0	1.3	4.3	1.5	0.0	2.1
J0007.0+7303	1.97	0.01	T	20.9	1.2	19.8	12.0	0.3	60.5	49.0	1.3	82.3	135.6	6.5	57.6	8.5	1.6	15.3
J0008.3+1452	2.00	0.21	⋯	0.9	0.0	0.0	0.2	0.0	0.5	0.6	0.2	3.8	2.0	0.9	4.5	1.2	0.0	0.0
J0008.9+0635	2.28	0.22	⋯	1.6	0.0	0.3	0.5	0.0	3.1	0.5	0.0	1.0	2.2	1.0	4.0	1.5	0.0	2.9
J0009.1+5031	2.41	0.13	⋯	4.0	0.0	2.3	0.5	0.1	4.6	0.9	0.3	4.6	3.5	1.2	5.1	1.4	0.0	2.0
J0011.1+0050	2.51	0.15	⋯	1.2	0.0	0.0	0.4	0.1	4.8	0.5	0.2	4.1	1.7	0.0	0.3	0.9	0.0	0.0
J0013.1−3952	2.09	0.22	⋯	1.2	0.0	0.1	0.3	0.0	1.4	0.9	0.0	2.9	2.3	0.0	1.4	2.1	0.0	4.3

Note. — This table is published in its entirety in the electronic edition of the Astrophysical Journal Supplements. A portion is shown here for guidance regarding its form and content.

[a]In units of 10^{-8} photons cm^{-2} s^{-1}

[b]In units of 10^{-9} photons cm^{-2} s^{-1}

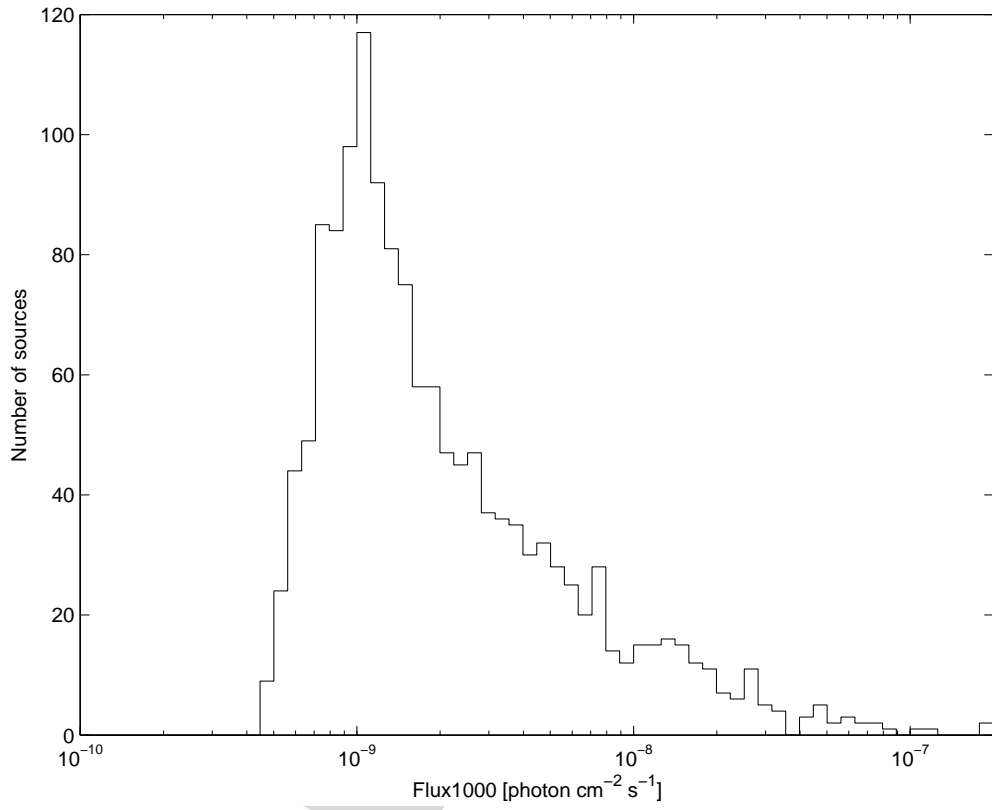[c]In units of 10^{-10} photons cm^{-2} s^{-1}

Fig. 16.— Distribution of the fluxes of the 1FGL sources, for energies in the energy range 1 GeV – 100 GeV.
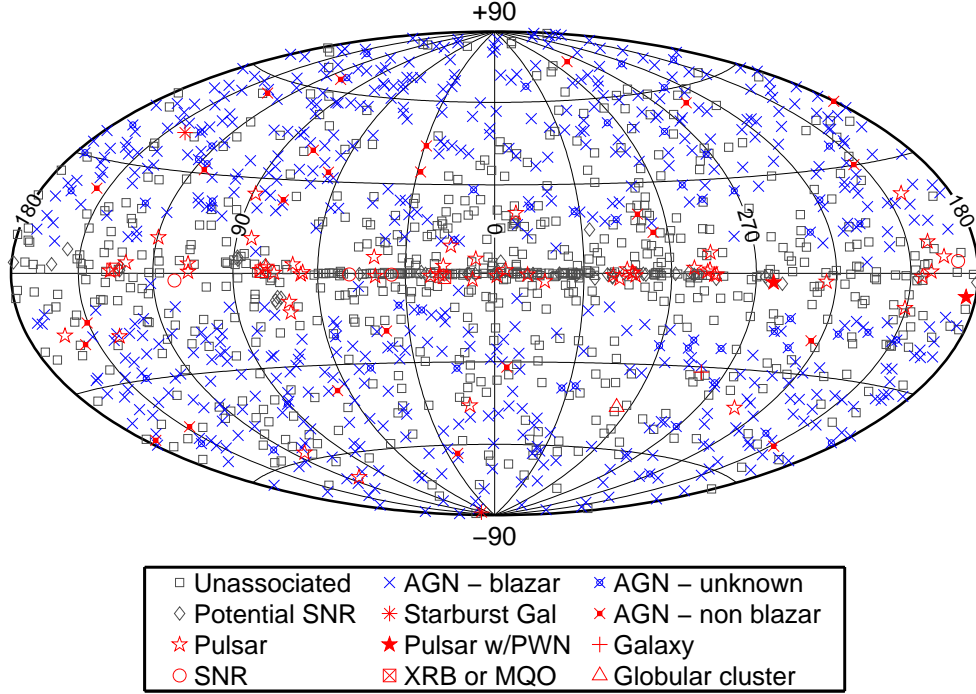
Fig. 17.— The 1451 1FGL catalog sources, showing locations on the sky (in Galactic coordinates with Aitoff projection) and associated source class, coded according to the legend. The color is chosen simply to enhance the visibility of the associated and non-blazar sources. For this plot the bzb, bzq and bzu designators have been combined ("AGN-blazar"), as have hxb and mqo ("XRB or MQO"). The sources possibly associated with SNR, PSR or PWN (those indicated by a dagger in Table 3) are listed as "Potential SNR".
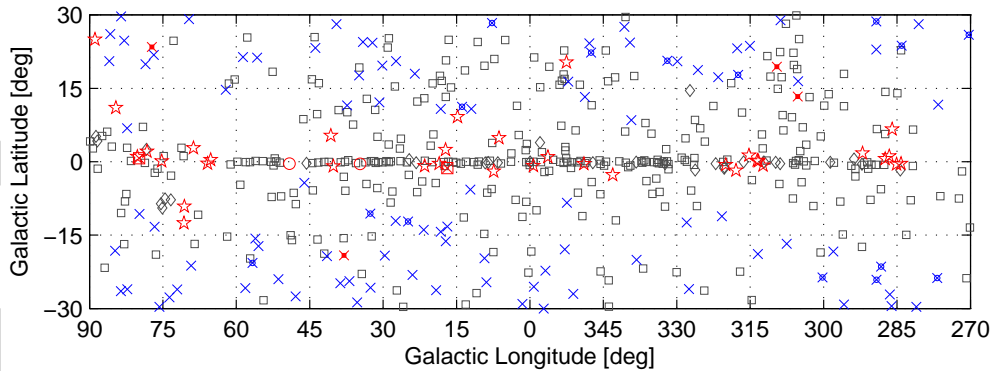

Fig. 18.— The 1FGL catalog sources in the inner Galactic region. Sources are indicated in the same manner as Figure 17.

Table 8. LAT First Catalog Columns

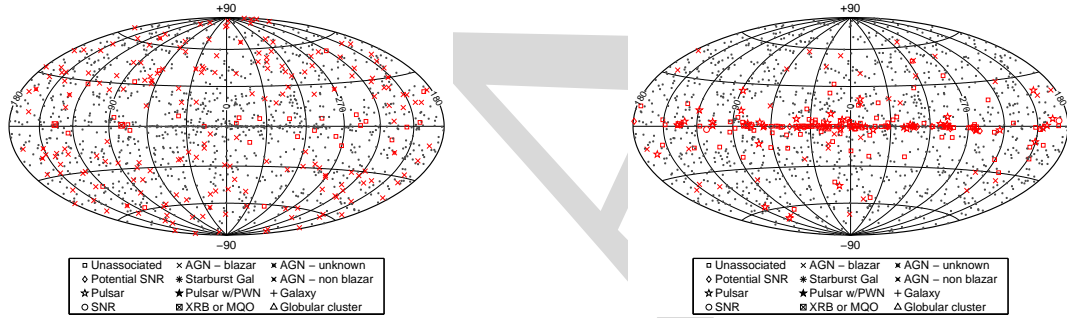| Column	Format	Unit	Description
Source_Name	18A		
RA	E	deg	Right Ascension
DEC	E	deg	Declination
GLON	E	deg	Galactic Longitude
GLAT	E	deg	Galactic Latitude
Conf_68_SemiMajor	E	deg	Long radius of error ellipse at 68% confidence
Conf_68_SemiMinor	E	deg	Short radius of error ellipse at 68% confidence
Conf_68_PosAng	E	deg	Position angle of the 68% long axis from celestial North, positive toward increasing RA (eastward)
Conf_95_SemiMajor	E	deg	Long radius of error ellipse at 95% confidence
Conf_95_SemiMinor	E	deg	Short radius of error ellipse at 95% confidence
Conf_95_PosAng	E	deg	Position angle of the 95% long axis from celestial North, positive toward increasing RA (eastward)
Signif_Avg	E		Source significance in sigma units (derived from Test Statistic)
Pivot_Energy	E	MeV	Energy at which error on differential flux is minimal
Flux_Density	E	$\mathrm{cm}^{-2}\ \mathrm{MeV}^{-1}\ \mathrm{s}^{-1}$	Differential flux at Pivot_Energy
Unc_Flux_Density	E	$\mathrm{cm}^{-2}\ \mathrm{MeV}^{-1}\ \mathrm{s}^{-1}$	1-sigma error on differential flux at Pivot_Energy
Spectral_Index	E		Best fit power law slope
Unc_Spectral_Index	E		1-sigma error on best fit power law slope
Flux1000	E	$\mathrm{cm}^{-2}\ \mathrm{s}^{-1}$	Integral flux from 1 to 100 GeV
Unc_Flux1000	E	$\mathrm{cm}^{-2}\ \mathrm{s}^{-1}$	1-sigma error on integral flux from 1 to 100 GeV
Energy_Flux	E	$\mathrm{erg\ cm}^{-2}\ \mathrm{s}^{-1}$	Energy flux from 100 MeV to 100 GeV
Unc_Energy_Flux	E	$\mathrm{erg\ cm}^{-2}\ \mathrm{s}^{-1}$	1-sigma error on energy flux from 100 MeV to 100 GeV
Curvature_Index	E		Measure of how spectrum follows power-law (currently simple χ^2)
Flux30_100	E	$\mathrm{cm}^{-2}\ \mathrm{s}^{-1}$	Integral flux from 30 to 100 MeV (not filled)
Unc_Flux30_100	E	$\mathrm{cm}^{-2}\ \mathrm{s}^{-1}$	1-sigma error on integral flux from 30 to 100 MeV (not filled
Sqrt_TS30_100	E		Square root of the Test Statistic between 30 and 100 MeV (not filled)
Flux100_300	E	$\mathrm{cm}^{-2}\ \mathrm{s}^{-1}$	Integral flux from 100 to 300 MeV
Unc_Flux100_300	E	$\mathrm{cm}^{-2}\ \mathrm{s}^{-1}$	1-sigma error on integral flux from 100 to 300 MeV))[a]
Sqrt_TS100_300	E		Square root of the Test Statistic between 100 and 300 MeV
Flux300_1000	E	$\mathrm{cm}^{-2}\ \mathrm{s}^{-1}$	Integral flux from 300 MeV to 1 GeV
Unc_Flux300_1000	E	$\mathrm{cm}^{-2}\ \mathrm{s}^{-1}$	1-sigma error on integral flux from 300 MeV to 1 GeV)[a]
Sqrt_TS300_1000	E		Square root of the Test Statistic between 300 MeV and 1 GeV
Flux1000_3000	E	$\mathrm{cm}^{-2}\ \mathrm{s}^{-1}$	Integral flux from 1 to 3 GeV
Unc_Flux1000_3000	E	$\mathrm{cm}^{-2}\ \mathrm{s}^{-1}$	1-sigma error on integral flux from 1 to 3 GeV)[a]
Sqrt_TS1000_3000	E		Square root of the Test Statistic between 1 and 3 GeV
Flux3000_10000	E	$\mathrm{cm}^{-2}\ \mathrm{s}^{-1}$	Integral flux from 3 to 10 GeV
Unc_Flux3000_10000	E	$\mathrm{cm}^{-2}\ \mathrm{s}^{-1}$	1-sigma error on integral flux from 3 to 10 GeV)[a]
Sqrt_TS3000_10000	E		Square root of the Test Statistic between 3 and 10 GeV
Flux10000_100000	E	$\mathrm{cm}^{-2}\ \mathrm{s}^{-1}$	Integral flux from 10 to 100 GeV
Unc_Flux10000_100000	E	$\mathrm{cm}^{-2}\ \mathrm{s}^{-1}$	1-sigma error on integral flux from 10 to 100 GeV)[a]
Sqrt_TS10000_100000	E		Square root of the Test Statistic between 10 and 100 GeV
Variability_Index	E		Measure of source variability (currently simple χ^2)
Signif_Peak	E		Source significance in peak interval in sigma units
Flux_Peak	E	$\mathrm{cm}^{-2}\ \mathrm{s}^{-1}$	Peak integral flux from 100 MeV to 100 GeV
Unc_Flux_Peak	E	$\mathrm{cm}^{-2}\ \mathrm{s}^{-1}$	1-sigma error on peak integral flux

Fig. 19.— The 1FGL catalog sources with variable (*left*) and spectrally-curved (*right*) sources highlighted. Sources with the variablity flag or spectral curvature flags set are shown according to their associated class, as red symbols, coded as marked as in the legend while sources showing no evidence of variability or with spectra compatible with power laws are shown as black dots.

6. Source Association and Identification

Even with the good angular resolution of LAT, source location accuracy is typically not precise enough to draw firm conclusions based on positional coincidence alone. A typical LAT error region contains numerous stars, galaxies, X-ray sources, infrared sources, and radio sources. Determination of the nature of a given LAT source must therefore rely on more information than simply location, including time variability, spectral information, and availability of sufficient energy and physical process at the source to produce γ-rays.

In this analysis, the LAT team makes a clear distinction between a source *identification* and an *association* with an object at another wavelength. A firm identification of a source is based on a timing characteristic such as a periodicity for a pulsar or binary or a variability correlated with observations at another wavelength in the case of a blazar, or on measurement of finite angular extent, which is the case for some Galactic sources, e.g., SNRs. An association is defined as a positional coincidence that is statistically unlikely to have occurred by chance between a plausible γ-ray-producing object and a LAT source.

For the 1FGL catalog, the approach to designating associations and identifications involves three steps:

1. A test for statistically-significant detections of classes of sources, based on a defined protocol as described by Torres & Reimer (2005) and Reimer (2007) has been carried out. Based on these results, some potential source classes are termed unlikely even if individual sources in such classes might be positionally coincident with 1FGL sources.

2. A general automated source association analysis, enhanced from the version used for the BSL (Abdo et al. 2009k), has been applied to the sources in the catalog. This method relies principally, although not exclusively, on comparing the local space density of plausible source classes with the number of positional associations found for a class with 1FGL sources.

3. For pulsars and binary systems with clearly-identified periodic emission, a firm identification can be established.

Each of these methods is described below.

6.1. Protocol for population identification

The idea for a protocol for population testing in gamma-ray source data such as represented by the *Fermi* 1st-year catalog was introduced by Torres & Reimer (2005), a paper to

which we refer for general background. The test was devised to provide high levels of confidence in population classification with small number statistics. Essential to this protocol is the use of Feldman & Cousins (1998) confidence level intervals in a priori, physically selected samples of plausible gamma-ray emitters.

Thus, we consider spatial correlations between the 1st-year catalog sources (1451 detections) and a priori selected (on physical grounds or earlier hints in gamma-ray data of previous missions) sets of astrophysical sources, details on which are given below. To test for spatial correlations, each of the *Fermi* source is described by a centroid position and an uncertainty. The latter is described by an ellipse, with semi-minor and semi-major axis and a position angle; with all these values being taken from the catalog at 95% CL. Those sources that are undoubtfully identified by timing (all gamma-ray pulsars and three X-ray binaries) have their positions assigned to be coincident with the corresponding astrophysical sources (as located in other wavelengths). However, for population searches, we maintain the uncertainty of their detections around these positions. In order to test systematics we also analyze the case in which all 1FGL sources have their positional uncertainties enlarged by increasing their corresponding semi-minor and semi-major axes by 20%. This is of course done consistently both for the real set of 1FGL sources, and for each of the simulated sets generated by Monte Carlo (see below), and it is just meant as a check of the results obtained with nominal uncertainty values.

Let $\mathcal{C}(A)$ represent the number of coincidences between candidate counterparts for population A and LAT sources. In case of finding the same *Fermi* detections spatially coincident with several astrophysical objects of the same class, we count all of the coincidences as one. An example of this is seen for millisecond pulsars pertaining to the same globular cluster, e.g., 47 Tuc. To determine the number of excess coincidences above the noise level, i.e., the sources that are expected to correlate by chance, we have to subtract the background b caused by these random coincidences, given the number and distribution of LAT sources and members of the testing population.

To obtain this latter number, we produce Monte Carlo simulations shuffling the orientation of the elliptical position uncertainty (but not its size) and the centroid position of each of the actual 1FGL sources, thus generating sets of fake LAT source detections. Each simulated 1FGL catalog is required to maintain the total number of sources (1451 detections), and both the longitude and latitude distributions of the real set. In order to obtain the most conservative results we proceed to simulate the fake LAT source detections maintaining the latitude (longitude) histogram of the real set with 5, and 10 (30, 60) degrees binning, and subsequently take the largest value for the expected average number of random positional coincidences among them (and this is called b). The number of excess detections above noise

will then be $\mathcal{E}(A) = \mathcal{C}(A) - b(A)$. This number will be used to test the null hypothesis: *Population A is not gamma-ray emitting at flux-levels detectable by the 1st-year LAT catalog.* The predicted signal events of this hypothesis is equal to 0, and the total expected events if this hypothesis is valid is equal to b. The further the real number of correlations is from the corresponding b-value for that population, the easier it will be to rule out the null hypothesis.

The testing power of a sample of finite size is limited: if using the same set of data, claiming the discovery of one population affects the level of confidence by which one can claim the discovery of a second. In order to control the reliability of our results, we will require that *the combination of all of our claims* be bounded by a probability of 10^{-5}, which then becomes the total budget $\mathcal{B}$. This low probability provides an overall significance of about 5σ, which implies individual claims of populations must arise with higher confidence. The total budget can then be divided into individual ones for each population, P_A, P_B, etc., such that $\sum_i P_i = \mathcal{B}$. Then, population A will be claimed as detected with x% CL if and only if:

- the Poissonian cumulative probability (CP) for obtaining the real number of (or more) spatial coincidences as a result of chance coincidence is less than the a priori assigned budget P_A (as opposed to be less only than the larger, total budget) and

- the number of excesses $\mathcal{E}(A)$ is beyond the upper limit of the corresponding confidence interval for x% CL, from Feldman & Cousins (1998).

The latter value, $x\%$, for each population is then the confidence level obtained using the tables in Feldman & Cousins (1998) for which the upper end of the interval equals the real number of excesses. (With number of events b, background b, recall that in the null hypothesis, there are 0 expected events above background.) The values of P for each population are chosen very conservatively: 0.01% B to each of the only two populations that were unambiguously identified in the EGRET catalog, pulsars and blazars; 0.1% B to millisecond pulsars and EGRET-coincident SNRs, which have been hinted at in the EGRET catalog; and the rest of the budget equally distributed into those classes where no high-energy gamma-ray emission was previously reported.

Finally, we provide brief notes on the populations selected for the test, recalling that this selection was made before the start of *Fermi* operations, as described in the internal LAT-document LAT-AM-09067[6], which lists each specific source selected in each class.

---

[6]Available from https://oraweb.slac.stanford.edu/pls/slacquery/DOCUMENTS.STARTUP?PROJECT=GLAST

- Blazars: The selected blazars are a subset of the CGRABS catalog (Healey et al. 2008), which is a uniform all-sky survey of EGRET-like blazars, selected by their Figure-of-merit (FoM) (see Healey et al. 2008). In total the CGRABS catalog includes 1625 sources. For assembling the testing list of blazars we cut the CGRABS catalog at the smallest FoM value where all high-condence EGRET blazars of the 3EG catalog (Hartman et al. 1999), which are also Mattox-blazars (Mattox et al. 2001), are included (see Sowards-Emmerd et al. 2003, for a comparison of 3EG and "Mattox"-blazars). This is then establishing a cut at FoM=0.111. A FoM cut at this value results in a total of 215 sources and constitutes the blazar list used for the application of the protocol.

- Misaligned jet sources: For this purpose we start with the compilation of Liu & Zhang (2002) of extragalactic jet sources which contains a total of 661 catalog members (December 2000) collected from the literature. This list contains radio galaxies, radio quasars, BL Lac objects and Seyfert galaxies. For a redshift cut at $z < 0.032$ (chosen to select a moderate number of the closest members of this class) the list features 51 sources: 34 are classied as radio galaxies (including all gamma-ray radio galaxies detected with high condence so far), 16 as Seyfert galaxies, and one as BL Lac object (not detected at gamma-rays so far and not included in the CGRABS list). 3C 111 and 3C 120 are added on the basis of evidence for their detection by EGRET.

- Starbursts: This list includes all starburst galaxies for which in the study of Torres et al. (2004) the combination of gas content, cosmic-ray density, and distance indicated a flux detectable by the LAT in one year.

- Halo Dwarf Galaxies: The list consists of presently-known objects in this category up to 1000 kly. This sample of Milky Way satellite galaxies is useful for probing localized γ-ray excesses due to annihilation of DM particles. Dwarf spheroidal galaxies (dSph) may be manifestations of the largest clumps predicted by the CDM scenario.

- Galaxy clusters: We restrict this sample to 30 clusters with the highest values of mass-to-distance-squared, M/d^2, from the the HIFLUCS sample of the Reiprich & Böhringer (2002) sample, complemented by clusters that are interesting individually (Bullet cluster, RX J1347.5), as well as those reported to have radio haloes. Galaxy clusters with reported hard X-ray emission, and those predicted from large scale structure formation simulations to be detectable by the LAT in one year (Pfrommer 2008) are implicitly included the sample constructed in this way.

- Pulsars: These are selected from the ATNF catalog (Manchester et al. 2005), with a cut on $\dot{E} > 10^{34}$ erg s^{-1}.

- Millisecond Pulsars: These are also selected from the ATNF catalog to have periods less than 10 ms), with the same cut as above in $\dot{E}$.

- Magnetars: We include all SGRs and AXPs known (13).

- EGRET-SNRs: These are all SNRs that were found to be spatially coincident with an EGRET source, as discussed by Torres et al. (2003a).

- TeV shell–type SNRs: these were intended to be tested separately to answer the question whether these objects also emit GeV gamma-rays on at least the level of the LAT 1 yr sensitivity. The sample comprised 4 sources (RX J1713.7−3946, RX J0852−460, RCW 86 and Cas A).

- Star-star binaries: These are from the VIIth WR catalog of van der Hucht (2001), requiring $0.001\, E_{kin,tot}/(4\pi d_L^2)) > 10$, resulting in a sample of 41 sources. The factor 0.001 is motivated by a reasonable 10% acceleration efficiency, i.e., wind-energy-to-relativistic-particle-energy-conversion efficiency, and 1% radiative efficiency in these environments, while the factor 10 relates to the LAT sensitivity anticipated at the time of protocol application.

- Star-compact object binaries: All gamma-ray binaries and microquasars known

- Binary pulsars: all objects known in this category

- Globular clusters: Globular clusters are known to contain a relatively large number of millisecond pulsars (MSPs) whose individual and collective emission in the X-ray and γ-ray energy bands may be detectable by LAT. Here the aim is to test for the collective emission from MSPs, since MSPs are principally able to accelerate leptons at the shock waves originated in collisions of the pulsar winds and/or inside pulsar magnetospheres, and inside a globular cluster these are subsequently able to Comptonize stellar and microwave background radiation. The globular clusters in this list are restricted to be closer than 6 kpc.

6.1.1. Protocol results

Table 9 summarizes the results of the application of the protocol for population identification to the 1FGL Catalog. To allow the sensitivity of the results to the sizes of the error ellipses for the sources, we also show results obtained when the extents of the ellipses are increased by a (very conservative) 20%. In the table, the first column (TP) shows the name of the test population. The second column (#) shows the number of astrophysical

objects included in the test of the population. The third column shows the expected number of random coincidences (or background, $b(A)$) between the N LAT sources included in the 1FGL catalog, and the number of astrophysical candidates in each population as explained above. The fourth column ($\mathcal{C}$) shows the real number of positional coincidences between the members of each population and the real LAT sources in the 1FGL catalog The fifth column shows the cumulative probability (CP) to obtain by chance coincidence a number of positional coincidences between LAT sources and the astrophysical candidates that is equal or larger than the number of actual matches $\mathcal{C}$. The sixth column shows the a priori assigned probability ($P(A)$) for discovery of each population, the sum of all P giving the total budget for population discovery. The seventh column answers yes or no to the question of whether the actual random probability for an equal or a larger number of excesses to occur by chance (CP) is larger than the a priori assigned budget for this population. For the cases in which this answer is yes, the last column gives the confidence level of the detection of the corresponding population; alternatively stated, this is the confidence with which we are ruling out the hypothesis that such a population is not present among the LAT detections (the null hypothesis).

Not surprisingly, the source populations conclusively identified already in the EGRET era are found with the highest confidence in the investigated 1FGL coincidences even when very strict thresholds were chosen for associations to be claimed, justifying a posteriori the very low budget assigned to these populations.

Spatial coincidences found between LAT sources and individual millisecond PSRs (MSPs) and those tested via their globular cluster environment are related in the following sense. Whereas for an isolated MSP there are not many alternative scenarios for producing detectable gamma-ray emission, and in fact several of them have been detected and identified by their gamma-ray periodicity, in the case of coincidences with globular clusters, an ambiguity exists as long as no pulsed emission from one of MSPs in the globular cluster is found. Thus, the aim was to search not only for the existence of a population of MSPs, but also to distinguish between environments in which MSPs are found as populations as well. The fact that the class of globular clusters is not detected as a population but the millisecond pulsars are can be interpreted as related to the size of the population of MSPs in a globular cluster. Based on the membership of the 1FGL catalog apparently only those clusters hosting a large number of MSPs were found coincident with catalog sources (e.g., Ter 5, 47 Tuc, M28) in a number too few for them to be claimed as a population of gamma-ray sources in the framework of this test.

Statistical evidence for the previously-reported relation between EGRET-sources and SNRs (e.g., Sturner & Dermer 1995; Torres et al. 2003b) is confirmed from the test with

1FGL sources, but the protocol finds them only as a population when the 20% enlargement of the uncertainty in position is considered. The latter is due to the low a priori assigned budget for the discovery of this population, which is narrowly missed using the nominal uncertainties. We do note that some of the SNRs in our sample have been detected as pulsars by the LAT, diluting the strength of the marginal detection claim.

The fact that the misaligned jet sources are found as a population supports the individual 1FGL source association findings, although the test did not distinguish between radio galaxies and Seyferts, and does not show a significant correlation with ranking via radio core flux. It is to be noted that this class is found only when the uncertainties in the positions of the LAT sources are not enlarged, when the cumulative probability is low, but found to be just below the a priori assigned budget for the class.

Starburst galaxies are detected as a population in LAT data, in numbers that add up to the noted individual detections of M82 and NGC 253, and suggests the potential for future discoveries.

Particularly interesting is the non-detection of galaxy clusters, which is not only a statistically significant result, it is in fact a zero coincidence case. With the absence of even a single galaxy cluster coincidence from the tested sample, we can conclude that X-ray bright nearby galaxy clusters and those exhibiting a radio halo do not constitute a source population above the 1FGL sensitivity limit: the models that we used to select the candidate globular clusters overestimate the energy conversation into particle acceleration at GeV and greater energies.

Dwarf Sphericals are not found coincident with LAT sources either. The result is compatible with the Null hypothesis that this population does not exist above the sensitivity limit of the catalog, although in some dark-matter-based models of their gamma-ray production they would have been expected to be seen at the sensitivity level of the 1FGL catalog. It is the same case for the Galactic populations of magnetars, binary pulsars, and WR binaries. The latter is particularly interesting, too; whereas positional associations of WR stars with LAT sources can be found using the extensive list of known WR stars, those having the largest wind energies do not present any correlation and thus we disregard WRs as gamma-ray emitters at the sensitivity limit of the 1FGL catalog.

Finally, it is interesting to note that whereas we found three sources correlated with MQ-gamma-ray binaries (all of them secured by timing) the population as such is not detected. We can conclude that the binaries identified in the 1FGL catalog are certainly special objects, but probably not archetypal for a population of similar objects. Similarly, the same occurs for TeV SNRs: we find some correlated objects, but not enough to claim a population discovery

due to the high value of b for this population.

6.2. Automated Source Associations

Our approach for automated source association follows closely the one used for the BSL, although we enlarged our database of catalogs of potential counterparts and we improved our calibration scheme to control more precisely the expected number of false associations. The association procedure, which follows essentially the ideas developed by Mattox et al. (1997) for the identification of EGRET sources with flat-spectrum radio sources, is described in detail in Appendices A and B. Here we only summarize the essential steps of the automated source association procedure.

The automated source association is based on a list of catalogs that contain potential counterparts of LAT sources. This list has been compiled based either on prior knowledge about classes of high-energy γ-ray emitters or on theoretical expectations. In total, 30 catalogs have been searched for counterparts covering AGN (and in particular blazars), nearby and starburst galaxies, pulsars and their nebulae, massive stars and star clusters, and X-ray binaries. In addition we search for counterparts at radio frequencies and TeV energies, and we search for coincidences between 1FGL sources and AGILE and EGRET sources. The complete list of catalogs, the number of objects they contain and the references are summarized in Table 10.

Table 8—Continued

Column	Format	Unit	Description
Time_Peak	D	s (MET)	Time of center of interval in which peak flux was measured
Peak_Interval	E	s	Length of interval in which peak flux was measured
Flux_History	nE	cm^{-2} s^{-1}	Integral flux from 100 MeV to 100 GeV in each interval
Unc_Flux_History	nE	cm^{-2} s^{-1}	1-sigma error on integral flux in each interval
0FGL_Name	18A		Name of corresponding 0FGL source if any
ASSOC_GAM1	18A		Name of likely corresponding 1AGL source
ASSOC_GAM2	18A		Name of likely corresponding 3EG source
ASSOC_GAM3	18A		Name of likely corresponding EGR source
CLASS1	3A		Class designation for associated source
CLASS2	3A		2nd class designation for associated source
ASSOC1	24A		Name of identified or likely associated source
ASSOC2	24A		Alternate name of identified or likely associated source
Flags	I		Source flags (binary coding as in Table 2)

[a]The upper limit is set equal to 0 if the flux in the corresponding energy band is an upper limit ($TS < 10$ in that band). The upper limits are 2-σ.

Table 9: Summary table for the application of the protocol. The first panel (up to the double line) shows results based on the reported position uncertainties for the 1FGL sources. The second panel (below the double line) shows results obtained if the extents of the position uncertainties are increased by 20%.

TP	#	b	$\mathcal{C}$	CP	P	(CP < P)?	CL
Galactic Populations tested							
Pulsars	215	1.440	30	5.3×10^{-29}	1.0×10^{-9}	yes	> 99.999%
Millisecond Pulsars	23	0.050	7	1.5×10^{-13}	1.0×10^{-8}	yes	99.89%
EGRET SNRs	23	1.590	13	1.5×10^{-8}	1.0×10^{-8}	no	$\cdots$
TeV SNRs	4	0.920	3	6.6×10^{-2}	9.9×10^{-7}	no	$\cdots$
Magnetars	13	0.120	0	$\cdots$	9.9×10^{-7}	$\cdots$	$\cdots$
WR-binaries	41	0.260	0	$\cdots$	9.9×10^{-7}	$\cdots$	$\cdots$
MQ/γ-ray bin.	17	0.140	3	4.1×10^{-4}	9.9×10^{-7}	no	$\cdots$
Binary pulsars	10	0.040	0	$\cdots$	9.9×10^{-7}	$\cdots$	$\cdots$
Globular clusters	29	0.240	4	1.1×10^{-4}	9.9×10^{-7}	no	$\cdots$
Extragalactic populations tested							
Blazars	215	0.480	61	0.0	1.0×10^{-9}	yes	> 99.999%
Misaligned jet sources	53	0.150	5	5.5×10^{-7}	9.9×10^{-7}	yes	99.25%
Starbursts	15	0.050	4	2.5×10^{-7}	9.9×10^{-7}	yes	97.89%
Galaxy clusters	48	0.150	0	$\cdots$	9.9×10^{-7}	$\cdots$	$\cdots$
Dwarf sphericals	18	0.070	0	$\cdots$	9.9×10^{-7}	$\cdots$	$\cdots$

TP	#	b	$\mathcal{C}$	CP	ap-P	(CP < ap-P)?	CL
Galactic Populations tested							
Pulsars	215	2.530	30	4.0×10^{-22}	1.0×10^{-9}	yes	> 99.999%
Millisecond Pulsars	23	0.090	7	8.7×10^{-12}	1.0×10^{-8}	yes	99.89%
EGRET SNRs	23	1.730	14	4.9×10^{-9}	1.0×10^{-8}	yes	> 99.998%
TeV SNRs	4	0.970	3	7.5×10^{-2}	9.9×10^{-7}	no	$\cdots$
Magnetars	13	0.160	0	$\cdots$	9.9×10^{-7}	$\cdots$	$\cdots$
WR-binaries	41	0.350	0	$\cdots$	9.9×10^{-7}	$\cdots$	$\cdots$
MQ/γ-ray bin.	17	0.210	3	1.3×10^{-3}	9.9×10^{-7}	no	$\cdots$
Binary pulsars	10	0.080	0	$\cdots$	9.9×10^{-7}	$\cdots$	$\cdots$
Globular clusters	29	0.320	4	3.3×10^{-4}	9.9×10^{-7}	no	$\cdots$
Extragalactic populations tested							
Blazars	215	0.680	63	0.0	1.0×10^{-9}	yes	> 99.999%
Misaligned jet sources	53	0.210	5	2.8×10^{-6}	9.9×10^{-7}	no	$\cdots$
Starbursts	15	0.060	4	5.1×10^{-7}	9.9×10^{-7}	yes	97.88%
Galaxy clusters	48	0.200	0	$\cdots$	9.9×10^{-7}	$\cdots$	$\cdots$
Dwarf sphericals	18	0.080	0	$\cdots$	9.9×10^{-7}	$\cdots$	$\cdots$

Table 10.   Catalogs Used for the Automatic Source Association and Results

Name	Objects	P_{prior}	N_{ass}	N_{false}	$\langle \hat{N}_{\mathrm{false}} \rangle$	Ref.
LAT pulsars	55	0.1	55	n.a.	0.4	1
High $\dot{E}/d^2$ pulsars	84	0.024	23	n.a.	0.6	2
Low $\dot{E}/d^2$ pulsars	1461	0.011	2	n.a.	0.3	2
Millisecond pulsars	139	0.278	20	n.a.	1.0	2
Pulsar wind nebulae	69	0.049	27	0.3	0.9	1
High-mass X-ray binaries	114	0.010	3	n.a.	0.3	3
Low-mass X-ray binaries	187	0.050	5	0.4	0.5	4
Point-like SNR	157	0.021	11	0.7	0.7	5
O stars	378	0.015	1	< 0.1	< 0.1	6
WR stars	226	0.013	2	0.3	0.2	7
LBV stars	35	0.026	2	0.3	0.6	8
Open clusters	1689	0.013	1	0.1	0.4	9
Globular clusters	147	0.272	8	< 0.1	0.5	10
Nearby galaxies	276	0.066	5	0.4	0.4	11
Starburst galaxies	14	0.5	2	< 0.1	< 0.1	12
Blazars (BZCAT)	2837	0.308	479	8.9	6.8	13
Blazars (CGRaBS)	1625	0.238	281	4.7	4.1	14
Blazars (CRATES)	11499	0.333	481	17.2	17.8	15
BL Lac	1122	0.224	217	2.8	2.8	16
AGN	21727	0.021	11	0.7	0.8	16
QSO	85221	0.166	140	7.3	4.9	16
Seyfert galaxies	16343	0.041	24	2.0	1.6	16
Radio loud Seyfert galaxies	29	0.1	4	< 0.1	< 0.1	1
Radio Fundamental Catalog	4558	0.266	478	11.5	10.1	17
TeV source catalog	120	0.037	43	0.6	1.1	18
Extended SNR†	117	n.a.	47	n.a.	18.1	5
Dwarf galaxies†	14	n.a.	7	n.a.	2.1	1
1st AGILE catalog*	40	n.a.	52	n.a.	18.6	19
3rd EGRET catalog*	271	n.a.	111	n.a.	25.4	20
EGR catalog*	189	n.a.	66	n.a.	9.1	21

References. — [1]Collaboration internal; [2]Manchester et al. (2005); [3]Liu et al. (2006); [4]Liu et al. (2007); [5]Green (2009); [6]Maíz-Apellániz et al. (2004); [7]van der Hucht (2001); [8]Clark et al. (2005); [9]Dias et al. (2002); [10]Harris (1996); [11]Schmidt et al. (1993); [12]Thompson et al. (2007); [13]Massaro et al. (2009); [14]Healey et al. (2007); [15]Healey et al. (2008); [16]Véron-Cetty & Véron (2006); [17]Kovalev (2009b) and ref. therein, http://astrogeo.org/vlbi/solutions/2009c_astro/; [18]http://tevcat.uchicago.edu/; [19]Pittori et al. (2009); [20]Hartman et al. (1999); [21]Casandjian & Grenier (2008).

For each catalog in the list, we make use Bayes' theorem to compute the posterior probabilities P_{ik} that an object i from the catalog is the correct association of the LAT source k:

$$P_{ik} = \left(1 + \frac{1 - P_{\text{prior}}}{P_{\text{prior}}} \frac{\pi \rho_k a_k b_k}{2.996} e^{\Delta_k}\right)^{-1}. \tag{10}$$

P_{prior} is the prior probability that counterpart i is detectable by the LAT, a_k and b_k are the semimajor and semiminor axes of the 95% confidence error ellipse, ρ_k is the local counterpart density around source k, and

$$\Delta_k = 2.996 \frac{r^2}{\Psi^2} \tag{11}$$

where

$$\Psi = \left(a_k^{-2} \cos^2(\theta - \phi_k) + b_k^{-2} \sin^2(\theta - \phi_k)\right)^{-1/2} \tag{12}$$

is the effective 95% confidence error radius for a given position angle θ between LAT source k and the counterpart i, ϕ_k being the position angle of the error ellipse, and r being the angular separation between LAT source k and counterpart i (see Appendix A). For each catalog, prior probabilities were P_{prior} assigned so that

$$N_{\text{false}} = \sum_{P_{ik} \geq P_{\text{thr}}} (1 - P_{ik}) \tag{13}$$

gives for a given catalog the number of false associations that have posterior probabilities above the threshold P_{thr} (see Appendix B). The corresponding prior probabilities are quoted in Table 10 (column 3) for all catalogs.

For the automated association of the 1FGL catalog we set $P_{\text{thr}} = 0.8$, which means that each individual association has a chance of $\leq 20\%$ for being spurious. This is different from the approach we took for the BSL paper where we constrained the number of false associations for each catalogue to $N_{\text{false}} \leq 1$, which imposed a relatively tight constraint on source classes with large numbers of associations (such as blazars and pulsars) while source classes with only few associations had a relatively loose constraint. Now, each individual association stands on an equal footing by having a well defined probability for being spurious.

For a number of catalogs in our list the Bayesian method cannot be applied since either (1) the location uncertainty of the counterpart is larger than the location uncertainty for the LAT source (these catalogs are marked by * in Table 10), or (2) the counterpart is an extended source (these catalogs are marked by † in Table 10). In the first case, we consider all objects i as associations for which the separation to the LAT source k is less than the quadratic sum of the 95% confidence error radius of counterpart i and the semimajor axis a_k. In the second case, we assume that the counterparts have a circular extension and consider all objects i as associations for which the circular extension overlaps with a circle of radius a_k around the LAT source k.

6.2.1.   Automated association summary

The results of the automated association procedure for each of the 30 catalogs are summarized in Table 10. For each catalog, we given the number

$$N_{\mathrm{ass}} = \sum_{P_{ik} \geq P_{\mathrm{thr}}} 1 \tag{14}$$

of LAT sources that have been associated to objects to a given catalog (column 4). Furthermore, we compute the number of false associations N_{false} using Eq. (13) for those catalogs which have been associated with the Bayesian method (column 5). We cannot give meaningful results for pulsars and high-mass X-ray binaries since for identified objects the positions have been fixed in the catalog to their true locations (§ 4), and consequently, their posterior probabilities are by definition 1. However, we alternatively estimated the expected number of false associations using Monte Carlo simulations of 100 realizations of fake LAT catalogs, for which no physical associations with counterpart catalog objects are expected (see Appendix B). We quote the resulting estimates $\langle \hat{N}_{\mathrm{false}} \rangle$ in column 6 of Table 10. We find $N_{\mathrm{false}} \approx \langle \hat{N}_{\mathrm{false}} \rangle$ which confirms that the posterior probabilities computed by the automatic association procedure are accurate (otherwise Eq. (13) would not hold).

In total we find that 829 of the 1451 sources in the 1FGL catalog (57%) have been associated with a least one counterpart by the automated procedure. 788 1FGL sources (54%) have been associated using the Bayesian method while the remaining 41 sources are spatial coincidences based on overlap of the error regions or source extents. From simulations we expect that 57.3 among the 829 sources (7%) are associated spuriously. Considering only the Bayesian associations, 37.5 among the 775 sources (5%) are expected to be spurious. In the following we discuss the automated association results is some detail.

6.2.2.   Blazars

Our association procedure contains 4 catalogs to cover the blazar source class (BZCAT, CGRaBS, CRATES, BL Lac) which have a substantial number of objects in common. In total we find 653 1FGL sources associated with sources from at least one of the 4 blazar catalogs. 2 of these sources (1FGL J0047.3−2512 and 1FGL J0956.5+6938) are the starburst galaxies M 82 and NGC 253 (both found in the CRATES catalog), and 2 sources (1FGL J0319.7+4130 and 1FGL J1325.6−4300) are the radio galaxies NGC 1275 and Cen A. This leaves 649 blazar candidates among the 1FGL sources.

We further note that 282 of the 1FGL sources associated with blazars also have counterparts in the VLBA calibrator survey (VCS) which we added to our list of catalogs following

the suggestion of Kovalev (2009a) who found 111 associations for this catalog among the BSL sources. For 47 of the 478 1FGL sources associated with VCS objects, the VCS association is the only counterpart found among all catalogs. Most of these 47 sources are located at low Galactic latitudes, a region where our 4 blazar catalogs are incomplete. Many of the low-latitude VCS associations thus may be related to blazars situated close to the Galactic plane (Kovalev 2009a).

6.2.3. Other AGNs

We find a total number of 26 1FGL sources that are associated with objects from the two Seyfert galaxy catalogues. Among those, only 4 sources are not also associated to blazars: 1FGL J0128.6+4439 (87GB 01257+4423) - also a CLASS source, 1FGL J0840.8+1310 (3C 207.0), 1FGL J0905.1−5736 (PKS 0903−57), and 1FGL J1230.8+1223 (M 87; Abdo et al. 2009d). 87GB 01257+4423 (Marlow et al. 2000) and PKS 0903−57 (Massardi et al. 2008) are flat-spectrum radio sources and both may indeed be blazars, while 3C 207.0 and M 87 are nearby radio galaxies **to be checked/validated/extended by AGN group**.

147 of the 1FGL sources are associated with AGN and QSO from the catalog of Véron-Cetty & Véron (2006), yet only 3 of them are not also associated to blazars: 1FGL J0250.4+1715 (RXS J02506+1712), 1FGL J0648.7−1740 (MC 0646-176), and 1FGL J2325.5−3559 (CTS A13.10). RXS J02506+1712 is classified as BL Lac (Laurent-Muehleisen et al. 1999) and the low-latitude source MC 0646-176 has also a VCS counterpart, so both may also be blazars.

Thus it appears that most of the 1FGL non-blazar associations are either sources that are in fact blazars, yet they are not classified as such in our catalogs, or they are nearby radio galaxies. In particular, we do not find convincing evidence for coincidences of 1FGL sources with non-blazar Seyfert galaxies **to be checked/validated/extended by AGN group**.

6.2.4. Normal Galaxies

We find 2 associations with nearby starburst galaxies (Abdo et al. 2009b) 1FGL J0047.3-2512 (NGC 253), and 1FGL J0956.5+6938 (M 82). Both galaxies have also been detected at TeV energies (Acero et al. 2009a) and (VERITAS Collaboration 2009) and hence can be considered as high-confidence 1FGL associations.

Seven 1FGL sources are found to coincide with dwarf galaxies: 6 are associated to the Large Magellanic Cloud (LMC), 1 is associated to the Small Magellanic Cloud (SMC),

both galaxies being extended. It is likely that these sources correspond to local maxima of extended emission features and probably they do not represent real point sources in the field. The exception is 1FGL J0600.7−7037 which is also associated to CRATES J060106−703606, a blazar that has shown significant time variability through the observing period (Abdo et al. 2009c).

Thus NGC 253, M 82, the LMC, and the SMC are so far the only normal galaxies that have been associated to sources in the 1FGL catalog.

6.2.5.   Pulsars, pulsar wind nebulae and globular clusters

Our association procedure correctly associates the 55 pulsars that have been identified as such through their γ-ray pulsations. In addition, we find 3 more associations with high $\dot{E}/d^2$ pulsars from the ATNF catalog: 1FGL J1119.4−6127 (PSR J1119−6127), 1FGL J1410.3−6128 (PSR J1410−6132), and 1FGL J1648.4−4609 (PSR J1648−4611) **N.B. This is not a 'dagger' source yet in the mane source table**. These 3 sources are obviously good candidates for young energetic γ-ray pulsars, although 1FGL J1119.4−6127 is also associated to the TeV pulsar wind nebula G292.2−0.5 and the supernova remnant G292.2−00.5 (see Table 6).

Among the 27 1FGL sources that are associated to pulsar wind nebulas (PWNs), only 6 are not also associated to known pulsars: 1FGL J1134.8−6055 (PWN G293.8+0.6), 1FGL J1552.4−5609 (G326.3−1.8), 1FGL J1635.7−4715 (G337.2+0.1), 1FGL J1640.8−4634 (G338.3−0.0),
1FGL J1745.6−2900, the Galactic center source (G359.95−0.04), and 1FGL J1746.4−2849 (G0.13−0.11). It remains to be shown whether the LAT indeed detects these pulsar wind nebulas, or whether the γ-ray emission arises from the yet-unknown pulsars that power the nebulas. Because of the ambiguity we do not list positional associations with PWNs or pulsars in the main source table (Table 3) but do include them in Table 6.

Among the 20 1FGL sources that are associated to millisecond pulsars, 11 are not associated to known γ-ray pulsars. Among those 11, 5 are associated to globular clusters and the remaining 6 may indeed be Galactic field γ-ray millisecond pulsars: 1FGL J0610.7−2059 (PSR J0610−2100), 1FGL J1024.6−0718 (PSR J1024−0719), 1FGL J1600.7−3055 (PSR J1600−3053), 1FGL J1713.9+0750 (PSR J1713+0747),
1FGL J1811.3−1959 (PSR J1810−2005), and 1FGL J1959.6+2047 (PSR B1957+20).

Finally, we find that 8 1FGL sources are associated to globular clusters. None of those have alternative associations different to millisecond pulsars or low-mass X-ray bi-

naries (which both are known source populations residing in globular clusters), which makes the reality of these associations even more plausible.

6.2.6. Supernova remnants

Our automated association procedure associates 58 1FGL sources with supernova remnants. Of those, 11 are associated to point-line SNRs while 47 are associated to extended SNRs.

From the 11 1FGL sources associated with point-like SNRs, only 5 have no concurrent pulsar associations: 1FGL J1134.8−6055 (G293.8+00.6, also associated to PWN G293.8+0.6), 1FGL J1213.7−6240 (G298.6−00.0), 1FGL J1617.5−5105 (G332.4−00.4), 1FGL J1640.8−4634 (G338.3−00.0, also associated to PWN G338.3−0.0, and 1FGL J2323.4+5849 (G111.7−02.1, aka Cas A; Abdo et al. 2010e). Except for 1FGL J2323.4+5849 and possibly 1FGL J1213.7−6240, the presence of alternative associations to PWNs or a low-mass X-ray binary make the physical association of these sources to supernova remnants questionable.

For the 47 1FGL sources associated to extended supernova remnants, the simulations indicate that many of them may indeed be spurious. However, some of the associations have already been suggested earlier based on morphology analyses of the LAT sources: 1FGL J1801.3−2322 (G006.4−00.1, aka W28), 1FGL J1856.1+0122 (G034.7−00.4, aka W44; Abdo et al. 2010f), 1FGL J1922.9+1411 (G049.2−00.7, aka W51C; Abdo et al. 2009g), and 1FGL J0617.2+2233 (G189.1+03.0, aka IC 443; Abdo et al. 2010g). Further interesting associations due to the presence of OH masers in the SNR (Hewitt et al. 2009) are 1FGL J1805.2−2137 and 1FGL J1806.8−2109 (both overlapping G008.7−00.1, aka W30).

6.2.7. Association of 1FGL J1745.6−2900 with the Galactic center

With a position $(l, b) = (359.941°, -0.051°)$ and a 95% confinement radius of 1.1′, 1FGL J1745.6−2900 is the source closest to the Galactic center. In this direction, many catalogs contain objects and consequently we find a large number of formal associations to this source. Specifically, 1FGL J1745.6−2900 is formally associated to the pulsar wind nebula G359.95−0.04, the supernova remnant G000.0+00.0, the VCS object J1745−2900, 4 low-mass X-ray binaries, 6 LBV stars, and 10 Wolf-Rayet stars and 2 TeV sources. We are of course unable to distinguish on basis of our association scheme among these possibilities, although some are more plausible physically. Eventually, the spectral energy distribution of the source or any characteristic time-variability may help in the future to narrow down the

possibilities.

6.2.8. X-ray binaries

We associate 3 1FGL sources with high-mass X-ray binaries (HMXB), and all of them have indeed identified by their orbital modulations as such: 1FGL J0240.5+6113 (LS I+61°303; Abdo et al. 2009h), 1FGL J1826.2−1450 (LS 5039; Abdo et al. 2009l), and 1FGL J2032.4+4057 (CygX-3; Abdo et al. 2009m).

Formally, we associate 5 1FGL sources with low-mass X-ray binaries (LMXB). 3 of them are also associated to globular clusters, and hence their combined emission from millisecond pulsars appears to be the more plausible counterpart of the 1FGL sources (see section 6.2.5). One association corresponds to the Galactic Center source (cf. section 6.2.7). And the remaining association 1FGL J1617.5−5105 (1E 161348−5055.1) is also associated to the supernova remnants G332.4−00.4. Thus, none of the LMXB associations gives strong evidence that we indeed detect gamma-ray emission from this source class.

6.2.9. O stars, Wolf-Rayet stars, LBV stars and open clusters

The automated association procedure finds one O star (Cyg OB2-4) associated to 1FGL J2032.2+4127, yet this source is known to be a γ-ray pulsar (PSR J2032+4127, Abdo et al. 2009n,a). In this case, the unusual large density of O stars in the Cyg OB2 association (Knödlseder 2000) leads to source confusion, and ignoring this association we do not find any evidence for γ-ray emission from O stars in the 1FGL catalog.

Formally, 2 1FGL sources were associated to Wolf-rayet stars. The first is the Galactic center source 1FGL J1745.6−2900, which, as stated above, has many possible alternative associations, so we definitely cannot establish a physical link between the LAT source and the Wolf-Rayet stars. The second is 1FGL J2032.4+4057 which has been identified as Cyg X-3 (Abdo et al. 2009m). Cyg X-3 is compact binary system that indeed comprises a Wolf-Rayet star, hence here the association is indeed correct. Yet it is not believed that the γ-ray emission is indeed arising from the Wolf-Rayet star (Abdo et al. 2009m), thus we also do not find any evidence for γ-ray emission from Wolf-Rayet stars in the 1FGL catalog.

Two 1FGL sources were associated to LBV stars: 1FGL J1745.6−2900, the Galactic center source, which for the same reason as given above we do not consider as a relevant association, and 1FGL J1746.4−2849, which is associated to FMM 362 and the Pistol Star. However, the latter source is concurrently associated to the pulsar wind nebula G0.13−0.11,

so also here it is difficult to establish a physical link.

Finally, we note that the LBV star η Carinae has not been formally associated by our procedure to the nearby source 1FGL J1045.2−5942. The formal posterior association probability for η Carinae is 0.76, hence below our threshold (0.8) for listing an association. The angular separation is 1.7′ which is slightly larger than the 95% containment radius of 1.4′. Thus η Carinae falls just outside the 95% error radius of 1FGL J1045.2−5942. On the other hand, 1FGL J1045.2−5942 has been associated to the open cluster Trumpler 16 (the only association to an open cluster for the 1FGL catalog), which besides η Carinae houses many massive stars, similar to the Cyg OB2 association. Recently, the young energetic pulsar PSR J2032+4127 was found by the LAT in Cyg OB2 (see above) and it is possible that young energetic pulsars are also hidden in Trumpler 16.

6.2.10. Associations with EGRET and AGILE sources

The sources in the 1FGL catalog match in position 107 of the 271 3EG sources (Hartman et al. 1999). (Four 3EG sources are each resolved into two 1FGL sources) and 66 of the 188 EGR sources (Casandjian & Grenier 2008). A few more of the EGRET sources are close to, but not formally consistent with, 1FGL source locations; the EGRET positions for the bright pulsars were offset from the true positions, for example. Almost all of the AGNs labeled in the 3EG catalog as good candidates are seen by LAT. One example exception is 3EG J1230−0247 (EGRc J1233−0318), which was seen only early in the CGRO mission.

The 1FGL catalog clearly does not account for a large fraction of the sources seen by EGRET. In light of the high sensitivity of the LAT and the fact that the LAT sees most of the EGRET catalog AGNs, which are known to be variable, the absence of more EGRET sources from the LAT catalog cannot be attributed primarily to time variability. A more likely explanation would seem to be that many of the EGRET sources were not discrete sources but were diffuse structures not included in the model of Galactic diffuse emission used for analysis of the EGRET data. Its improved angular resolution and high photon statistics at GeV energies make the LAT far less sensitive to such structures, and the diffuse model itself has incorporated far more detail than was available in the EGRET era. See § 4.7, however, for a discussion of how even some 1FGL sources may be affected by the modeling of the diffuse gamma-ray emission.

All 47 of the sources in the first AGILE catalog (Pittori et al. 2009) have corresponding sources in the 1FGL catalog. A number of the 1AGL sources map to multiple 1FGL sources, and a few of the 1AGL sources are close but not formally consistent in position with the

1FGL sources. Nevertheless, the two operating high-energy gamma-ray telescopes do appear to be consistent in their detections of bright sources.

6.3. Firm Identifications

Firm identifications, indicated in the main table by capitals in the Class column, require more than a high-probability positional association. The strongest test for identification is time variability, either periodicity or correlation with variability seen at another wavelength. The 55 pulsars that have Class PSR all show high-confidence (statistical probability of chance occurrence less than 10^{-6}) periodicity caused by the rotation of the neutron star (Abdo et al. 2009n, 2010a,b). Similar confidence levels apply to the three X-ray binary systems whose orbital periods are detected in the LAT data: LSI +61 303 (Abdo et al. 2009h), LS5039 (Abdo et al. 2009l), and Cygnus X-3 (Abdo et al. 2009m).

With the large number of LAT blazar detections and the significant variability seen in many of these, the search for correlated variability that can provide firm identifications is a major effort that has not yet been carried out systematically for the LAT data. We have therefore chosen to list as firm identifications only those blazars for which publications exist showing such variability. Additional studies will undoubtedly expand this list.

Another approach to firm identification, slightly less robust than time variability, is morphology: finding spatial extent in a gamma-ray source that matches resolved emission at other wavelengths. The Large Magellanic Cloud (LMC) is an example (Abdo et al. 2009c) that illustrates the issue of analyzing an extended source with tools designed to find point sources. The location and flux of 1FGL J0538.9−6914 do not reflect the total gamma-ray emission from the LMC, but only a localized region. Nevertheless, the LMC can be considered a firmly identified LAT source. Several supernova remnants also show measurable spatial extent and can be considered firm identifications. The same qualifier applies to these as to the LMC in terms of comparing flux and location of a resolved source with the analysis performed assuming pointlike emission. A special case is 1FGL J1322.0−4515, which appears to be part of one of the lobes of the emission from radio galaxy Centaurus A (Abdo et al. 2010c). Studies of source morphology are ongoing.

7. TeV Source Associations

1FGL sources that are positionally associated with sources seen by TeV telescopes are of particular interest because the TeV band overlaps with the LAT energy range, suggesting the

potential for such sources to be physically related. Although this catalog makes no attempt to carry out physical modeling needed to demonstrate such connections, we present the associations between 1FGL and TeVCat sources in Table 11, along with a few associations with published TeV sources that are not yet in TeVCat, and comment on some of these associations.

1. The LAT PSR 1FGL J1023.0−5746 is spatially consistent with HESS J1023−575, itself not yet firmly identified, but noted for its possible connection to the young stellar cluster Westerlund 2 in the star-forming region RCW49 (Aharonian et al. 2007).

2. 1FGL J1119.4−6127 is a candidate pulsar (PSR J1119−6127) spatially coincident with the newly discovered HESS J1119−614, a candidate PWN at TeV energies; in this case the positional association could indeed be in reality a physical association.

3. 1FGL J1503.4−5805 is consistent with HESS J1503−582 (Renaud et al. 2008).

4. 1FGL J1614.7−5138 is consistent with HESS J1614−518 (Aharonian et al. 2006), one of the brightest (∼25% of Crab flux) H.E.S.S. unidentified sources.

5. 1FGL J1648.4−4609 is consistent with a very large (∼1 deg) newly discovered source, consistent with the Star Forming Region (SFR) Westerlund 1 (Ohm et al. 2009)

6. 1FGL J1702.4−4147 also could represent an interesting case, since it lies in the "tail" of the unidentified source HESS J1702−420 (Aharonian et al. 2008b).

7. 1FGL J1707.9−4110 is spatially consistent with HESS J1708−410 (Aharonian et al. 2008b) and hence it represents the first plausible counterpart for the TeV γ-ray source.

8. 1FGL J1803.1-2147 and 1FGL J1805.2−2137 are compatible with HESS J1804−216 (Aharonian et al. 2006), a slightly extended (22′) unidendified TeV gamma-ray source.

9. 1FGL J1839.1−0543 is consistent with the very large and complicated unidentified source HESS J1841−055 (Aharonian et al. 2008b).

10. 1FGL J1844.3−0309 is consistent with the rather extended unidentified source HESS J1843−033 (The H. E. S. S. Collaboration 2007).

11. 1FGL J1848.1−0145 is consistent with HESS J1848−018 (Chaves et al. 2008), that is suspected to be correlated with the SFR W 43.

Table 11.   Associations of 1FGL Sources with TeVCat

Name 1FGL	TeVCat name[a]
J0047.3−2512	NGC 253
J0222.6+4302	3C66A
J0240.5+6113	LSI +61 303
J0319.7+1847	RBS 0413
J0416.8+0107	1ES 0414+009
J0507.9+6738	1ES 0502+675
J0534.5+2200	Crab
J0710.6+5911	RGB J0710+591
J0721.9+7120	S5 0716+714
J0809.5+5219	1ES 0806+524
J0956.5+6938	M82
J1015.1+4927	1ES 1011+496
J1103.7−2329	1ES 1101-232
J1104.4+3812	Markarian 421
J1119.4−6127	HESS J1119-614
J1136.6+7009	Markarian 180
J1221.3+3008	1ES 1218+304
J1221.5+2814	W Comae
J1230.8+1223	M87
J1256.2−0547	3C279
J1325.6−4300	Centaurus A
J1426.9+2347	PKS 1424+240
J1428.7+4239	H 1426+428
J1555.7+1111	PG 1553+113
J1640.8−4634	HESS J1640-465
J1653.9+3945	Markarian 501
J1709.7−4429	PSR B1706-44
J1745.6−2900	GalCentreRidge
J1745.6−2900	GalCentreRidge
J1800.5−2359	HESS J1800-240B
J1826.2−1450	LS 5039
J1833.5−1034	HESS J1833-105
J1837.5−0659	HESS J1837-069
J1922.9+1411	HESS J1923+141
J1959.6+2047	PSR B1957+20
J2000.0+6508	1ES 1959+650
J2009.5−4849	PKS 2005-489
J2021.5+4026	0FGL J2021.5+4026
J2158.8−3013	PKS 2155-304
J2202.8+4216	BL Lacertae
J2229.0+6114	Boomerang
J2323.4+5849	Cassiopeia A
J2347.1+5142	1ES 2344+514
J2359.0−3035	H 2356-309

[a]http://tevcat.uchicago.edu/

The association between GeV γ-ray PSRs and the PWNe visible in TeV γ-rays seems well established, as has already been discussed in Abdo et al. (2009n). Blazars, particularly BL Lac objects are also solidly connected between the GeV and TeV energy ranges (Abdo et al. 2009j), as are two starburst galaxies (Abdo et al. 2009b), and the HMXB sources LSI +61 303 (Abdo et al. 2009h) and LS5039 (Abdo et al. 2009l). Supernova remnants such as W51C (Abdo et al. 2009g) and Cas A (Abdo et al. 2010e) also connect the two energy regimes.

As discussed in Section 6.2.7, the Galactic Center region is particularly complex. Investigations of the associations with the TeV gamma-ray sources known in this region – HESS J1745-290 (Acero et al. 2009b), HESS J1745-303 (Aharonian et al. 2008a) and HESS J1741-302 (Tibolla et al. 2008) are outside the scope of this paper and will be discussed elsewhere.

Sources of particular interest are those that are positionally consistent between the LAT and TeV telescopes but have no obvious associations with objects at longer wavelengths. Establishing a physical connection through spectral or variability studies may help determine the nature of these sources. Sources in this category include the following:

All of these represent good candidates for detailed multiwavelength studies.

8. Conclusion

The 1451 sources in this First *Fermi* LAT Catalog (1FGL) represent the most complete understanding to date of sources in the GeV sky. The catalog clearly contains a number of populations of γ-ray emitters. It offers a multitude of opportunities for additional research, both on sources with likely associations or identifications and on those sources that remain without apparent counterparts.

Facilities: Fermi LAT.

REFERENCES

Abdo, A. A., et al. 2008, Science, 322, 1218

—. 2009a, Science, 325, 840

—. 2009b, arXiv:0911.5327

—. 2009c, A&A, in press (FERMI LAT OBSERVATIONS OF THE LMC)

—. 2009d, ApJ, 707, 55

—. 2009e, Physical Review Letters, 103, 251101

—. 2009f, ApJ, 696, 1084

—. 2009g, ApJ, 706, L1

—. 2009h, ApJ, 701, L123

—. 2009i, Science, 323, 1688

—. 2009j, ApJ, 707, 1310

—. 2009k, ApJS, 183, 46

—. 2009l, ApJ, 706, L56

—. 2009m, Science, 326, 1512

—. 2009n, arXiv:0910.1608

—. 2009o, Astroparticle Physics, 32, 193

—. 2010a, ApJ, submitted (PSR J0034-0534)

—. 2010b, ApJ, submitted (EIGHT GAMMA-RAY PULSARS DISCOVERED IN BLIND SEARCHES BY FERMI LAT)

—. 2010c, Science, in press (CEN A LOBES)

—. 2010d, ApJ, 708, 1254

—. 2010e, ApJ, submitted (CASSIOPEA A)

—. 2010f, Science, in press (doi:10.1126/science.1182787)

—. 2010g, ApJ, submitted (IC 443)

—. 2010h, ApJ, in press (SPECTRAL PROPERTY OF BRIGHT AGN)

—. 2010i, ApJ, submitted (THE FIRST FERMI LAT CATALOG OF AGN)

Acero, F., et al. 2009a, Science, 326, 1080

—. 2009b, MNRAS, 1915

Aharonian, F., et al. 2005, Science, 307, 1938

—. 2006, ApJ, 636, 777

—. 2007, A&A, 467, 1075

—. 2008a, A&A, 483, 509

—. 2008b, A&A, 477, 353

Atwood, W. B., et al. 2009, ApJ, 697, 1071

Benjamini, Y., & Hochberg, Y. 1995, Journal of the Royal Statistical Society, Series B, 57, 289

Camilo, F., et al. 2009, ApJ, 705, 1

Campana, R., Massaro, E., Gasparrini, D., Cutini, S., & Tramacere, A. 2008, MNRAS, 383, 1166

Casandjian, J.-M., & Grenier, I. A. 2008, A&A, 489, 849

Chaves, R. C. G., Renaud, M., Lemoine-Goumard, M., & Goret, P. 2008, in American Institute of Physics Conference Series, Vol. 1085, American Institute of Physics Conference Series, ed. F. A. Aharonian, W. Hofmann, & F. Rieger, 372–375

Ciprini, S., et al. 2007, in American Institute of Physics Conference Series, Vol. 921, The First GLAST Symposium, ed. S. Ritz, P. Michelson, & C. A. Meegan, 546–547

Clark, J. S., Larionov, V. M., & Arkharov, A. 2005, A&A, 435, 239

Damiani, F., Maggio, A., Micela, G., & Sciortino, S. 1997, ApJ, 483, 350

Dias, W. S., Alessi, B. S., Moitinho, A., & Lépine, J. R. D. 2002, A&A, 389, 871

Feldman, G. J., & Cousins, R. D. 1998, Phys. Rev. D, 57, 3873

Giveon, U., Becker, R. H., Helfand, D. J., & White, R. L. 2005, AJ, 130, 156

Green, D. A. 2009, Bulletin of the Astronomical Society of India, 37, 45

Harris, W. E. 1996, AJ, 112, 1487

Hartman, R. C., et al. 1999, ApJS, 123, 79

Healey, S. E., Romani, R. W., Taylor, G. B., Sadler, E. M., Ricci, R., Murphy, T., Ulvestad, J. S., & Winn, J. N. 2007, ApJS, 171, 61

Healey, S. E., et al. 2008, ApJS, 175, 97

Helene, O. 1983, Nuclear Instruments and Methods in Physics Research, 212, 319

Hewitt, J. W., Yusef-Zadeh, F., & Wardle, M. 2009, ApJ, 706, L270

Knödlseder, J. 2000, A&A, 360, 539

Kovalev, Y. Y. 2009a, ApJ, 707, L56

Kovalev, Y. Y. 2009b, in Astronomical Society of the Pacific Conference Series, Vol. 402, Astronomical Society of the Pacific Conference Series, ed. Y. Hagiwara, E. Fomalont, M. Tsuboi, & M. Yasuhiro, 179–+

Laurent-Muehleisen, S. A., Kollgaard, R. I., Feigelson, E. D., Brinkmann, W., & Siebert, J. 1999, ApJ, 525, 127

Liu, F. K., & Zhang, Y. H. 2002, A&A, 381, 757

Liu, Q. Z., van Paradijs, J., & van den Heuvel, E. P. J. 2006, A&A, 455, 1165

—. 2007, VizieR Online Data Catalog, 346, 90807

Maíz-Apellániz, J., Walborn, N. R., Galué, H. Á., & Wei, L. H. 2004, ApJS, 151, 103

Manchester, R. N., Hobbs, G. B., Teoh, A., & Hobbs, M. 2005, AJ, 129, 1993

Marlow, D. R., Rusin, D., Jackson, N., Wilkinson, P. N., Browne, I. W. A., & Koopmans, L. 2000, AJ, 119, 2629

Massardi, M., et al. 2008, MNRAS, 384, 775

Massaro, E., Giommi, P., Leto, C., Marchegiani, P., Maselli, A., Perri, M., Piranomonte, S., & Sclavi, S. 2009, A&A, 495, 691

Mattox, J. R., Hartman, R. C., & Reimer, O. 2001, ApJS, 135, 155

Mattox, J. R., Wagner, S. J., Malkan, M., McGlynn, T. A., Schachter, J. F., Grove, J. E., Johnson, W. N., & Kurfess, J. D. 1997, ApJ, 476, 692

Ohm, S., et al. 2009, in International Cosmic Ray Conference, Vol. 0947, International Cosmic Ray Conference

Pfrommer, C. 2008, MNRAS, 385, 1242

Pittori, C., et al. 2009, A&A, 506, 1563

Protassov, R., van Dyk, D. A., Connors, A., Kashyap, V. L., & Siemiginowska, A. 2002, ApJ, 571, 545

Rando, R., et al. 2009, arXiv:0907.0626

Reimer, A. 2007, ApJ, 665, 1023

Reiprich, T. H., & Böhringer, H. 2002, ApJ, 567, 716

Renaud, M., Goret, P., & Chaves, R. C. G. 2008, in American Institute of Physics Conference Series, Vol. 1085, American Institute of Physics Conference Series, ed. F. A. Aharonian, W. Hofmann, & F. Rieger, 281–284

Schlegel, D. J., Finkbeiner, D. P., & Davis, M. 1998, ApJ, 500, 525

Schmidt, K., Priebe, A., & Boller, T. 1993, Astronomische Nachrichten, 314, 371

Sowards-Emmerd, D., Romani, R. W., & Michelson, P. F. 2003, ApJ, 590, 109

Starck, J.-L., & Pierre, M. 1998, A&AS, 128, 397

Strong, A. W. 2007, Ap&SS, 309, 35

Strong, A. W., Moskalenko, I. V., & Reimer, O. 2004, ApJ, 613, 962

Sturner, S. J., & Dermer, C. D. 1995, A&A, 293, L17

Sutherland, W., & Saunders, W. 1992, MNRAS, 259, 413

The H. E. S. S. Collaboration. 2007, ArXiv e-prints

Thompson, D. J., Simpson, G. A., & Özel, M. E. 1981, J. Geophys. Res., 86, 1265

Thompson, D. J., et al. 1993, ApJS, 86, 629

Tibolla, O., Komin, N., Kosack, K., & Naumann-Godo, M. 2008, in American Institute of Physics Conference Series, Vol. 1085, American Institute of Physics Conference Series, ed. F. A. Aharonian, W. Hofmann, & F. Rieger, 249–252

Torres, D. F., & Reimer, O. 2005, ApJ, 629, L141

Torres, D. F., Reimer, O., Domingo-Santamaría, E., & Digel, S. W. 2004, ApJ, 607, L99

Torres, D. F., Romero, G. E., Dame, T. M., Combi, J. A., & Butt, Y. M. 2003a, Phys. Rep., 382, 303

—. 2003b, Phys. Rep., 382, 303

van der Hucht, K. A. 2001, New Astronomy Review, 45, 135

VERITAS Collaboration. 2009, Nature, 462, 770

Véron-Cetty, M.-P., & Véron, P. 2006, A&A, 455, 773

Weltevrede, P., et al. 2010, ApJ, 708, 1426

Wilks, S. S. 1938, Ann. Math. Stat., 9, 60

Wolstencroft, R. D., Savage, A., Clowes, R. G., MacGillivray, H. T., Leggett, S. K., & Kalafi, M. 1986, MNRAS, 223, 279

Wright, E. L., et al. 2009, ApJS, 180, 283

A. Association method

The method implemented for automatic association of the *Fermi*/LAT first year catalog sources essentially follows the ideas developed by Mattox et al. (1997) for the identification of EGRET sources with flat-spectrum radio sources. It makes use of Bayes' theorem to compute the posterior probability $P_{ik}(A|r,\theta)$ that a counterpart i from a list of potential counterparts supplied in the form of a *counterpart catalog* is the correct association of a *Fermi*/LAT source k:

$$P_{ik}(A|r,\theta) = \frac{p_{ik}(r,\theta|A)P_i(A)}{p_{ik}(r,\theta|A)P_i(A) + p_{ik}(r,\theta|\overline{A})P_i(\overline{A})}. \tag{A1}$$

$P_i(A)$ is the prior probability that counterpart i is detectable by the LAT, $P_i(\overline{A}) = 1 - P_i(A)$ is the prior probability that counterpart i is not detectable by the LAT, $p_{ik}(r,\theta|A)$ is the probability density for observing the detectable counterpart i at an angular separation r and position angle θ from a LAT source k, and $p_{ik}(r,\theta|\overline{A})$ is the probability density for source k being only by chance situated at an angular separation r and position angle θ from counterpart i.

The probability density $p_{ik}(r,\theta|A)$ is obtained by differentiation of the probability $P_{ik}(r,\theta|A)$ that the LAT source k being located at an angular separation smaller than r under the position angle θ:

$$p_{ik}(r,\theta|A) = \frac{d^2 P_{ik}(r,\theta|A)}{r\,dr\,d\theta}. \tag{A2}$$

By defining

$$\Delta_k = \ln\max(L_k) - \ln L_k(r,\theta) \tag{A3}$$

as the difference between the log-likelihood maximum of the LAT source k and the log-likelihood at position (r,θ) and by making use of Wilks's theorem that $2\Delta_k$ is distributed as χ_2^2 in the null hypothesis Wilks (1938) one can write

$$P_{ik}(r,\theta|A) = 1 - \int_{2\Delta_k}^{\infty} \chi_2^2(x)\,dx = 1 - e^{-\Delta_k}. \tag{A4}$$

We approximate Δ_k as an elliptical parabolid which is defined by the 95% confidence elliptical error region provided in the catalog and specified by the semimajor axis a_k (Conf_95_SemiMajor), the semiminor axis b_k (Conf_95_SemiMinor), and the position angle ϕ_k (Conf_95_PosAng):

$$\Delta_k = 2.996\,\frac{r^2}{\Psi^2} \tag{A5}$$

where

$$\Psi = \left(a_k^{-2}\cos^2(\theta - \phi_k) + b_k^{-2}\sin^2(\theta - \phi_k)\right)^{-1/2} \tag{A6}$$

is the effective 95% confidence error radius for a given position angle θ between LAT source k and the counterpart i (the coefficient 2.996 is such that the ellipse $r^2 = \Psi^2$ corresponds to the 95% confidence contour). By substituting $z = r/\Psi$ (Wolstencroft et al. 1986) one obtains $rdrd\theta = 2\pi a_k b_k z dz$ which results in

$$p_{ik}(r,\theta|\mathrm{A}) = \frac{2.996}{\pi a_k b_k} e^{-\Delta_k}. \tag{A7}$$

The chance coincidence probability density $p_{ik}(r,\theta|\overline{\mathrm{A}})$ is determined from the local density ρ_k of counterparts around LAT source k as proposed by Sutherland & Saunders (1992):

$$p_{ik}(r,\theta|\overline{\mathrm{A}}) = \frac{d^2 P_{ik}(r,\theta|\overline{\mathrm{A}})}{rdrd\theta} = \rho_k. \tag{A8}$$

To compute this density we count the number of counterparts N_k in the counterpart catalog under consideration within a radius of $r_0 = 4°$ around the location of the LAT source k and divide by the solid angle of the search region:

$$\rho_k = \frac{N_k}{\pi r_0^2} \tag{A9}$$

Note that the counterpart i is included in N_k which guarantees that $N_k \geq 1$.

As last step, we implement the reasonable condition that a counterpart i cannot be associated to more than one LAT source. This is done by introducing $N_{\mathrm{LAT}} + 1$ mutually exclusive hypotheses ($N_{\mathrm{LAT}} = 1451$ being the number of sources in the first year catalog):

H_k: Object i is a counterpart of LAT source k and of none of the other LAT sources.

H_-: Object i is not a counterpart of any LAT source.

The probabilities for these new hypotheses are computed using

$$\begin{aligned}
\tilde{P}_{ik}(\mathrm{H}_k|r,\theta) &= P_{ik}(\mathrm{A}|r,\theta) \prod_{k' \neq k} P_{ik'}(\overline{\mathrm{A}}|r,\theta) \\
\tilde{P}_i(\mathrm{H}_-|r,\theta) &= \prod_{k'} P_{ik'}(\overline{\mathrm{A}}|r,\theta).
\end{aligned} \tag{A10}$$

where

$$P_{ik}(\overline{\mathrm{A}}|r,\theta) = 1 - P_{ik}(\mathrm{A}|r,\theta). \tag{A11}$$

Since we dropped in the set of hypotheses here the cases where an object i is associated to more than a single LAT source, the sum over all probabilities

$$\tilde{S}_i = \sum_k \tilde{P}_{ik}(\mathrm{H}_k|r,\theta) + \tilde{P}_i(\mathrm{H}_-|r,\theta) \tag{A12}$$

is ≤ 1, and we thus renormalize using

$$P_{ik}(\mathrm{H}_k|r,\theta) = \frac{\tilde{P}_{ik}(\mathrm{H}_k|r,\theta)}{\tilde{S}_i} \tag{A13}$$

to obtain the posterior probability that object i is a counterpart of the LAT source k and of none of the other LAT sources. Practically, $\tilde{S}_i < 1$ only if the error ellipses of neighbouring LAT sources overlap, which is rather unlikely. Thus, is good approximation we have $P_{ik}(\mathrm{H}_k|r,\theta) = P_{ik}(\mathrm{A}|r,\theta)$ for basically all sources.

The above procedure that leads to the computation of $P_{ik}(\mathrm{H}_k|r,\theta)$ for a specific catalog of counterpart candidates has been implemented in the ScienceTools executable `gtsrcid`. We used version `v2r2p3` of this tool for counterpart association for the first year catalog. For simplification, we will write from now on P_{ik} instead of $P_{ik}(\mathrm{H}_k|r,\theta)$ for the posterior association probability of LAT source k with object i of a given counterpart catalog.

B. Calibration of posterior probabilities

Before Eq. (A1) can be used for source association, prior probabilities $P_i(\mathrm{A})$ have to be specified for each counterpart i, and a posterior probability threshold P_{thr} has to be defined above which associations are considered as valid. We make here the simplifying assumption that within a given counterpart catalogue the prior probabilities for all sources i are identical:

$$P_i(\mathrm{A}) = P(\mathrm{A}). \tag{B1}$$

To assign $P(\mathrm{A})$ for a given counterpart catalog, we require the relation

$$N_{\mathrm{false}} = \sum_{P_{ik} \geq P_{\mathrm{thr}}} (1 - P_{ik}) \tag{B2}$$

to hold, where N_{false} is the number of false associations that have posterior probabilities P_{ik} above a given threshold P_{thr}. For this purpose we first determine for each catalog P_{thr} as function of $P(\mathrm{A})$ that satisfy Eq. (B2) for a given value of N_{false}. We then determine by means of Monte Carlo simulations of fake LAT catalogs (which have no physical link to the sources in the counterpart catalog) the true number of false associations, $\langle \hat{N}_{\mathrm{false}} \rangle$, that we obtain as function of $P(\mathrm{A})$ when we use the corresponding P_{thr} values detemined above. Equating $N_{\mathrm{false}} = \langle \hat{N}_{\mathrm{false}} \rangle$ provides then the proper prior probability $P(\mathrm{A})$ for the counterpart catalog.

Figure 20 illustrates the procedure for the CRATES catalog of flat spectrum radio sources and using $N_{\mathrm{false}} = 1$ (we verified that to first order the resulting $P(\mathrm{A})$ value are

independent of the precise value of N_{false}). The left panel shows as red curve the posterior threshold P_{thr} as function of $P(A)$ that satisfies Eq. (B2) for $N_{\text{false}} = 1$. The black line shows the corresponding number of associations

$$N_{\text{ass}} = \sum_{P_{ik} \geq P_{\text{thr}}} 1. \tag{B3}$$

The right panel shows as red dots the average number of false associations, $\langle \hat{N}_{\text{false}} \rangle$, that was found in 100 simulations of fake LAT catalogs as function of $P(A)$. The solid red line represents of polynomial fit to these data points, and the intersection of this line with $\langle \hat{N}_{\text{false}} \rangle = 1$ defines the prior probability $P(A)$ that satisfies $N_{\text{false}} = \langle \hat{N}_{\text{false}} \rangle$. In this specific example we find $P(A) = 0.33$ for the CRATES catalog.

In order to illustrate how the fake LAT catalogs were generated, we show in Fig. 21 the locations of the sources in the 100 fake catalogues that were used for calibration. LAT sources were randomly displaced within a ring from $2°$ to $10°$ in radius around their nominal position. Since the 1FGL catalog includes a distinct population of Galactic sources that obey a rather narrow latitude distribution (see Sec. ??), we limit source displacement in Galactic latitude to $b \pm b_{\text{max}}$, where

$$b_{\text{max}} = r_{\text{max}} \left(1.0 - \text{sech}^2 \left(\frac{b}{b_0} \right) \right), \tag{B4}$$

$r_{\text{max}} = 10°$, b is the Galactic latitude of the LAT source, and $b_0 = 5°$ is the angular scale height above the Galactic plane for which the latitude displacement is reduced. We further require $b_{\text{max}} \geq 0.2°$ to allow for a non-zero latitude displacement of sources in the Galactic plane, and require any source to be shifted by at least $r_{\text{min}} = 2°$ away from its original location.

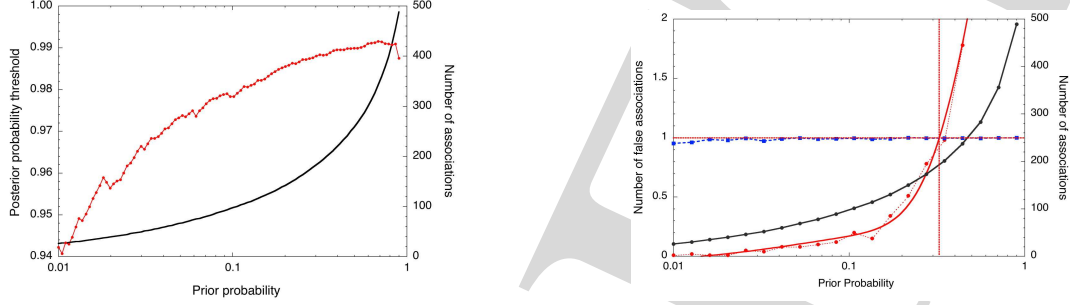Fig. 20.— Posterior probability threshold P_{thr} as function of prior probability $P(\mathrm{A})$ for $N_{\mathrm{false}} = 1$ (left panel), and $\langle \hat{N}_{\mathrm{false}} \rangle$ as function of $P(\mathrm{A})$ (right panel). The solid black lines show N_{ass} (right axis). In the right panel, the intersection of the red curve (which is a polynomial fit to the data points) with $\langle \hat{N}_{\mathrm{false}} \rangle = 1$ defines the prior probability $P(\mathrm{A})$ (red vertical line). The blue dots show N_{false} as determined using Eq. (B2) for the true LAT catalog as function of $P(\mathrm{A})$.
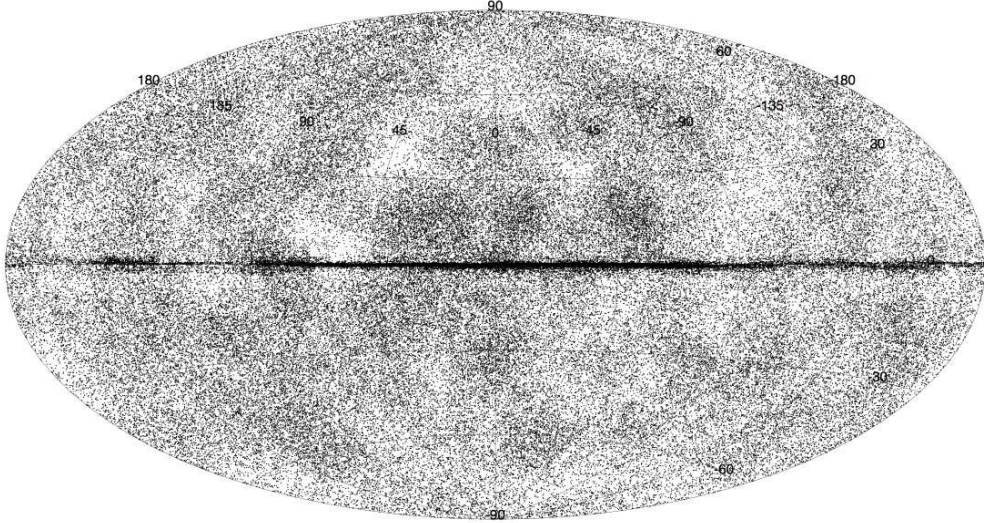

Fig. 21.— Locations of sources in the 100 fake LAT catalogs used for calibration of posterior probabilities.